Document Version
Final published version

Citation (APA)
Manoj, I., de Castro, D. B., Pascoe, J. A., & Alderliesten, R. (2026). Influence of process zone evolution on apparent mode II fracture characterization: Role of pre-crack and compliance in bonded joints. *Engineering Fracture Mechanics*, *342*, Article 112252. https://doi.org/10.1016/j.engfracmech.2026.112252

Engineering Fracture Mechanics 342 (2026) 112252

Contents lists available at ScienceDirect

Engineering Fracture Mechanics

journal homepage: www.elsevier.com/locate/engfracmech

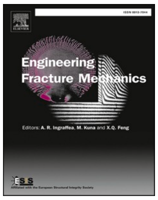

Influence of process zone evolution on apparent mode II fracture characterization: Role of pre-crack and compliance in bonded joints

Ishan Manoj *, Daniel Bernardes de Castro, John-Alan Pascoe, René Alderliesten

Aerospace Structure and Materials, Delft University of Technology, 2600 GB Delft, the Netherlands

ARTICLE INFO

Keywords:
Fracture toughness
Compliance
Pre-cracking
Damage evolution
Apparent crack length
Digital image correlation
Finite element analysis

ABSTRACT

This study investigates the influence of pre-crack conditions (introduced under Mode I and Mode II loading prior to fracture testing) and specimen compliance on the Mode II fracture characterization (G_{IIC}) of adhesively bonded composite joints. Calibrated End-Loaded Split (CELS) and 3-Point-Bending ENF tests were performed using structural AF163-2 K adhesive. Various data reduction schemes were employed to account for pre-crack morphology and compliance in the development of the R-curve. The data reduction schemes showed significant scatter, ranging from 8.07 ± 0.17 to 17.3 ± 1.19 N/mm, depending on the pre-cracking conditions and compliance effect. Mode I pre-cracked specimens consistently exhibit higher G_{IIC} values compared to Mode II pre-cracked specimens, a difference governed by the morphology and extent of the fracture process zone (FPZ). Mode I pre-cracking forms a localized FPZ that subsequently transitions into a shear-dominated FPZ for G_{IIC} evaluation during the subsequent Mode II fracture test. In contrast, Mode II pre-cracked specimens contain an already-developed shear FPZ that is broader and more diffuse, resulting in lower strain-energy release rates and lower G_{IIC} values. High compliance effects cause significant bending, additionally introducing high derogatory energy deformation from the test fixtures, obscuring the actual crack tip. The apparent crack length methods demonstrated reliable estimates of fracture energy and R-curve behavior by accounting for the effects of large FPZ, thereby capturing both crack-tip and distributed dissipation mechanisms. The experimental findings correlate with computational results, displaying stable cohesive disbond growth in the adhesive layer. This study indicates that pre-cracking and compliance effects significantly influence Mode II fracture characterization and, therefore, need to be properly addressed.

Abbreviations: ASTM, American Society for Testing and Materials; CBBM, Compliance-Based Beam Method; CBTE, Corrected Beam Theory with Effective crack length; CCM, Compliance Calibration Method (specific to ENF); CELS, Calibrated End-Loaded Split; CFRP, Carbon Fiber Reinforced Polymer; CZM, Cohesive Zone Modeling; DBT, Direct Beam Theory; DCB, Double Cantilever Beam; DIC, Digital Image Correlation; ECM, Experimental Compliance Method; ENF, End-Notch Flexural; FEA, Finite Element Analysis; FPZ, Fracture Process Zone; ISO, International Organization for Standardization; LEFM, Linear Elastic Fracture Mechanics; R-curve, Resistance curve (Fracture energy vs. crack extension); SBT, Simple Beam Theory; UD, Unidirectional.

* Corresponding author.
E-mail address: i.manoj@tudelft.nl (I. Manoj).

https://doi.org/10.1016/j.engfracmech.2026.112252
Received 26 January 2026; Received in revised form 22 April 2026; Accepted 8 May 2026

Nomenclature

Latin Symbols

a	Physically/Visually Observed Crack Length
a_0	Initial Crack length (from Teflon insert)
a_e	Effective Crack Length (used in CBTE)
a_f	Apparent Crack Length (used in CBBM)
a_P	*Pre-crack Length*
B	Specimen Width
C	*Compliance*
C_0	*Initial Compliance*
C_C	*Corrected Compliance*
C_{0C}	*Initial Corrected Compliance*
$E = E_{nn}$	Young's Modulus of Adhesive
E_{11}, E_{22}	Longitudinal and Transverse Modulus of the Laminate
E_f	Flexural Modulus of Adherend
E_{1f}	Apparent Flexural Modulus (used in CBBM)
$e1$ [1]	Major Principal Strain (from DIC software)
F	Large displacement Correction Factor
$G = E_{ss}$	Shear Modulus of Adhesive
G_{12}, G_{13}, G_{23}	In-Plane, Out-of-Plane, and Transverse Shear Modulus of Laminate
G_{IC}	Mode I critical Strain Energy Release Rate
G_{II}	Mode II Strain Energy Release Rate
G_{IIC}	Mode II critical Strain Energy Release Rate
h	Thickness of a Single Specimen Arm
I	Second Moment of Inertia
L	Free length/Span Length
L_0	Initial Free Length
m	Slope of the Compliance vs. a^3 Curve
M	Bending Moment
N	End-block Correction Factor
P	Applied Load
t	Adhesive Thickness
U	Strain Energy

Greek Symbols

δ	Displacement
Δ_{clamp} (or Δ)	Clamp Correction Factor for CELS
Δ_I	Correction Factor for Crack Length in Mode I
Δ_{II}	Crack Length Correction for Mode II
η	Mixed-mode Interaction Parameter (BK law)
$\theta_{1..5}$	Geometric Variables for Calculating F and N
μ	Coefficient of Friction
υ_{12}, υ_{13}, υ_{23}	*Poisson's Ratios of Laminate in Respective Direction*
σ_n	Normal Cohesive Strength
σt	Shear Cohesive Strength
s	Viscosity Stabilization Parameter

1. Introduction

Adhesively bonded joints have several advantages over mechanical fastening and riveting [1,2]. They reduce structural weight, provide better stress distribution, and cause less damage to the adherends compared to drilling a hole for fasteners [3,4]. In practical applications, load transfer between substrates occurs through a combination of loading modes. The dominant mechanisms are Mode I (tensile opening) and Mode II (in-plane shear). Mode I behavior is typically characterized using the Double Cantilever Beam (DCB) test, whereas Mode II response is evaluated through methods such as the Calibrated End-Load Split (CELS), three-point bending End-Notch Flexure (ENF), and four-point bending ENF tests [5].

Adhesively bonded joints are designed to maximize in-plane shear loading, promoting crack propagation in a constrained manner parallel to the bonded interface through sufficient overlap length [6,7]. Yet, Mode II fracture characterization remains challenging due to the inherent difficulties in real-time crack-tip monitoring, the sensitivity of the energy release rate calculations to specimen compliance, and the development of a fracture process zone (FPZ) that is significantly larger than that observed in Mode I. Furthermore, results are influenced by discrepancies in experimental test configurations, such as the clamping effect or the fixture-induced friction, and the selection of analytical data reduction schemes used to interpret the load–displacement data [8,9].

While ASTM and ISO standards [10,11] provide well-established guidelines for Mode II delamination characterization in fiber-reinforced composites, no standardized procedures currently exist for Mode II fracture characterization for adhesively bonded joints. This gap is due to the difference in the size and morphology of FPZ formed in adhesive layer, which is different from that formed in interlaminar delamination. Hence, it becomes imperative to properly address the factors influencing the fracture characterization of adhesives [12].

Mode II fracture characterization has been explored previously; however, the primary difficulty lies in the poor reproducibility of

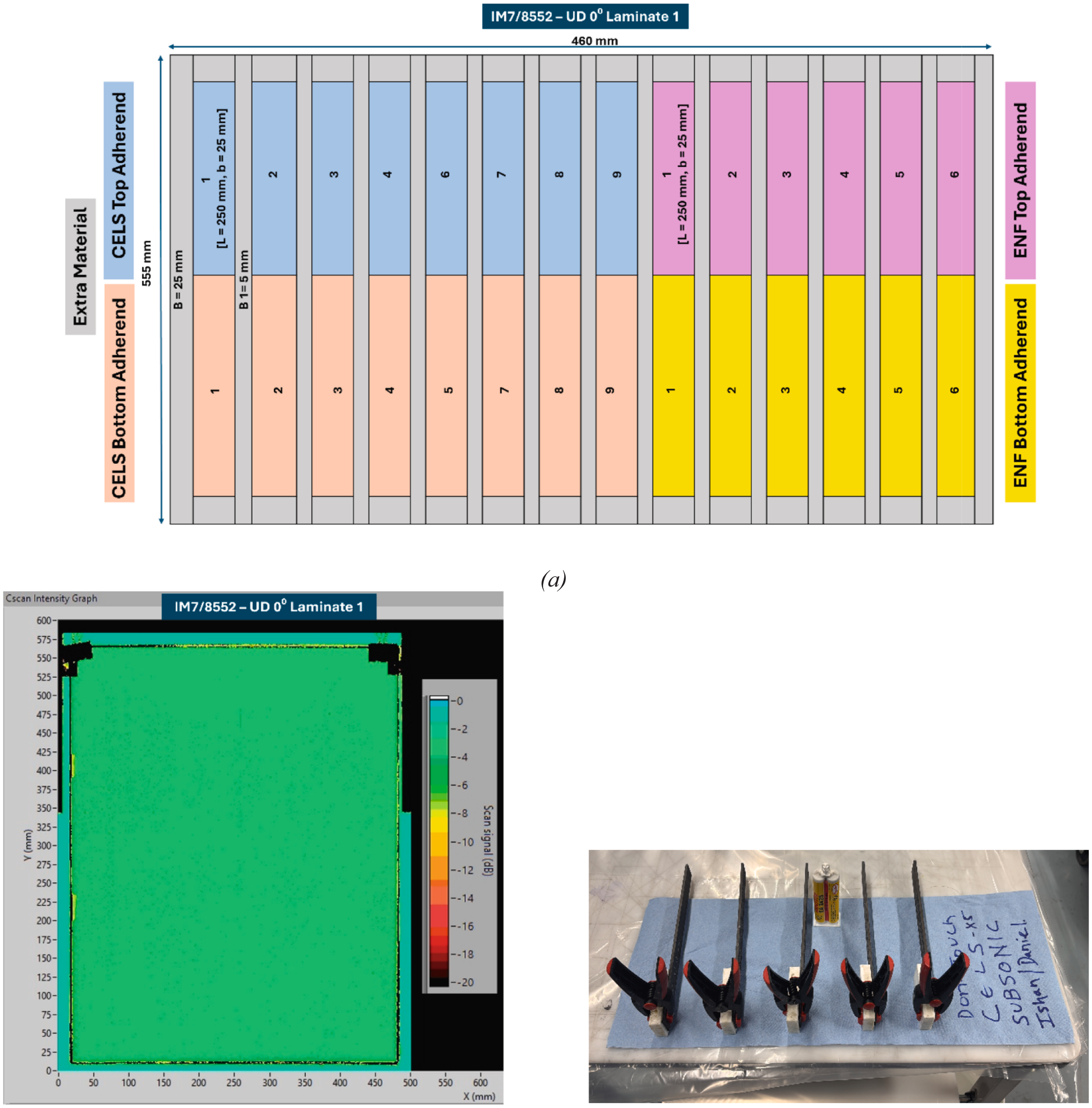

(a)

(b)

(c)

Fig. 1. (a) Representation of Lay-out for laminate preparation of CELS and ENF specimens (b) C-Scan performed to ensure build-up quality of laminates (c) Attachment of End-block to CELS specimens.

fracture toughness and the factors that influence it [13–16]. Carlsson et al. [17] reported that friction between roller and specimen in the ENF test can produce a difference in measured mode II critical strain energy release rate (G_{IIC}). The sensitivity in choosing the data reduction schemes for measuring G_{IIC} should account for the fixture-induced friction effect [18,19]. For instance, the classical data reduction scheme depends on the precise measurement of the real-time crack tip, which is highly sensitive to its location [20]. However, it is very difficult to accurately locate the actual crack tip in mode II due to the large FPZs and due to absence of a crack opening line such as in pure Mode I tests [15,21].

To address this limitation, Blackman et al. [15,22] proposed an apparent crack length method that incorporates compliance calibration to account for variations in flexural modulus. Similarly, De Moura et al. [23–25] introduced the effective crack length method, which also utilizes the apparent flexural modulus to improve the accuracy of Mode II fracture characterization. Sarrado et al. [26] found that data decomposition based on the J-integral is a good alternative to Linear Elastic Fracture Mechanics (LEFM) when large FPZs are present. Similarly, several studies have proposed that the J-integral closed-form solution can be a better alternative to other available data reduction schemes [27–29]. Despite these findings, literature reveals substantial variability in the reported Mode II fracture toughness of adhesives. For example, studies on the structural film adhesive AF163-2 K have shown an extensive range of G_{IIC} values, varying from 0.67 N/mm to 17.8 N/mm [28,30–36]. Additionally, it is often unclear why G_{IIC} values selected for validation in numerical models differ from those obtained through experimental characterization [36]. Moreover, challenges still remain in achieving stable crack propagation and convergence in the R-curve, especially for toughened adhesives [37,38].

ASTM D7905 [10] and ISO 15114 [11] explicitly state that a pre-crack may be introduced in either Mode I or Mode II to facilitate stable crack propagation. Typically, a sharp pre-crack is employed to ensure such stability. However, a notable gap exists in literature concerning the influence of this pre-cracking, despite its potentially significant effect on the formation and evolution of the FPZ [39,40]. Furthermore, it remains unexamined whether identical pre-cracking modes applied across different test configurations yield consistent material properties. For example, some studies indicate that the CELS test provides more favorable conditions for achieving stable crack growth compared to the three-point ENF test, implying the results may not be directly transferable [41,42].

It is noted that strict Linear Elastic Fracture Mechanics (LEFM) applicability requires a small-scale damage zone relative to the specimen dimensions, a condition more readily satisfied in Mode I (e.g., DCB) configurations [29,45–48]. In contrast, Mode II fracture in toughened adhesive systems is typically associated with a relatively large FPZ [15,23,24,40]. Despite this, several studies have demonstrated that energy-based fracture parameters remain consistent, with the strain energy release rate (G) showing strong agreement with nonlinear J-integral evaluations [26,36,49]. Therefore, the use of LEFM-based energy concepts in conjunction with appropriate data reduction schemes remains a valid and widely accepted approach for Mode II characterization [14,22,50].

The objective of the present study was to investigate the influence of the pre-cracking condition (introduced under Mode I or Mode II loading prior to fracture testing) on the determination of G_{IIC} and development of the FPZ, using two test configurations having different compliance characteristics, along with a comparison of multiple data-reduction schemes. Finally, finite-element analysis (FEA) exploiting cohesive zone modeling (CZM) was employed to correlate with experimental findings, effectively replicating the fracture process and enabling the estimation of fracture toughness [43,44].

The outcomes of this work provide valuable insights into the role of pre-cracking across different test configurations with varying compliance and establish a correlation between data reduction schemes and the evaluation of Mode II fracture toughness.

2. Experiments

2.1. Materials and manufacturing

The laminates were manufactured using 16 plies of unidirectional HexPly IM7/8552 prepreg, with a nominal fiber volume fraction of 57.70% (as indicated in the data sheet) [51]. The lay-up plan, as illustrated in Fig. 1a, representatively displays the geometry of the laminates from which the adherends were cut. The laminates were manufactured using the hand lay-up process, with vacuum debulking applied after each alternate ply. The length of the adherend was 250 mm, and its width was 25 mm.

The laminates were cured in an autoclave according to the manufacturer's recommendations at an absolute pressure of 7 bar and a maximum temperature of 180 °C for 7 h [51]. A C-scan was performed on the laminate to ensure the quality of the manufactured composite (Fig. 1b). The thickness of the laminate was calculated by averaging 5 points on each side: $t \approx 2.16 \pm 0.09$ mm. The top and bottom adherends of the CELS and ENF specimens were cut from the laminate using a comp-cut ACS 600 cutting machine using a cutting disc and water as a coolant, before being bonded together. The surface of the composites was carefully abraded using fine-grit sandpaper (P120) along the fiber direction [52]. The surface was then cleaned with a fresh cotton cloth soaked in isopropanol. The structural film adhesive AF163-2 K was employed for bonding the adherends [28,30–36].

Recent work by Sun et al. [28,36] investigated this adhesive using thick adherends. In contrast, the present study utilized comparatively thinner adherends made of a different material, following a unidirectional (UD) lay-up to account for compliance effects and evaluate the source of property discrepancies using the same adhesive. This approach also enables a more consistent comparison for determining the intrinsic material properties of the adhesive. An initial crack of 70 mm was created for CELS and ENF specimens using a very thin (≈ 0.1 mm) Teflon insert. The top and bottom adherends of bonded CELS and ENF assembly were again autoclaved according to the manufacturer's curing recommendation at a differential pressure of 3.5 bar and a maximum temperature of 130 °C for 2 h [53]. The bonded composite laminates were then precisely cut to the required specimen geometry. The thickness of the adhesive layer after curing was measured using an optical microscope, which was $\approx 0.17 \pm 0.02$ mm. The end blocks for the CELS specimens were grit blasted and cleaned with acetone. Finally, the end blocks were bonded to the CELS samples and left to cure at room temperature for 48 h (Fig. 1c). A minimum of three samples for each test were manufactured to ensure repeatability.

2.2. Test Set-Up

The ENF and CELS tests were performed on a Zwick static testing machine equipped with a 1 or 10 kN load cell. The tests were conducted in a displacement-controlled setup with a quasi-static rate of 0.5 mm/min. The test setup for the ENF and CELS tests is depicted in Fig. 2. A high-resolution camera was positioned on one side to track the propagation of the crack (Camera 1). One lateral side of the specimens was painted white, and then, using a sharp knife with a ≈ 0.1 mm nib, marks were made at regular intervals of 1 mm for the initial 10 – 20 mm of length from the crack tip, 2.5 mm for the next 10–20 mm of length, and 5 mm for remaining specimen length up to the clamp. Similarly, a high-resolution Digital Image Correlation (DIC) camera, was used to monitor changes in the speckle pattern from the other side [54]. Very fine speckles were painted on the specimens on the DIC camera's side to form trackable patterns.

The DIC helped in obtaining a full-field strain field and displacement map, while camera 1 provided complementary visual crack tracking, enabling the accurate measurement of disbond growth. A third high-resolution camera (camera 2) was installed to monitor the displacement and rotation of the end block attached to the machine. All three cameras were synchronized with the controller of the Zwick machine for the force and displacement readings. Pictures for crack tracking and DIC were taken at an interval of 3 s, while the third camera recorded the movement after consecutive 10-second intervals. Sufficient light sources were used to illuminate the test environment, reducing the scatter of outside lighting. All tests were conducted under laboratory conditions at 22 °C and 60% relative humidity.

2.2.1. Pre-cracking and geometric details for CELS

Two sets of specimens were prepared to introduce controlled pre-crack conditions prior to Mode II fracture testing. The distinction between Mode I and Mode II pre-cracks in this study refers exclusively to the method used to generate the initial crack, and not to the subsequent fracture loading mode.

For the first set, pre-cracks were introduced under Mode I loading conditions using a controlled opening procedure similar to a Double Cantilever Beam (DCB) configuration. This approach promotes crack initiation under tensile-dominated conditions, resulting in a relatively sharp crack tip with limited shear-induced damage.

For the second set, pre-cracks were generated under Mode II loading conditions, producing a shear-dominated crack front with a more developed local damage zone at the crack tip.

Following pre-crack introduction, all specimens were tested under Mode II loading conditions, using either the CELS or ENF configurations to evaluate the Mode II fracture response. This approach enables a direct assessment of how the initial pre-crack condition influences the subsequent fracture behavior and the measured apparent Mode II fracture toughness.

The initial crack length“a_0”, measured from the point of load application, was approximately 60 ± 1 mm. Mode II pre-cracking introduction was conducted at a loading rate of 0.5 mm/min, followed by unloading at a rate of 5 mm/min, as specified in ISO 15114 [11]. The initial free length “L_0”, for pre-cracking, was selected based on a ratio of “$a_0/L_0 = 0.8$”, resulting in a relatively short span.

To control crack extension within the range of 2–5 mm, 2.5 mm markings were made on the specimen. The test was stopped when the vertical lines had shifted beyond the first 2.5 mm marking and slightly before the 5 mm markings. Visual inspection indicated that the new initial crack length, “a_P”, was approximately 63.5 ± 1.5 mm. For the final testing phase, a longer free length was adopted to obtain a fully developed R-curve. The new free length, $L = 95\ mm$, corresponded to a ratio of “$a_P/L = 0.66$”. To introduce Mode I pre-cracks, both adherends of the specimen were pulled in tension, producing a sharp pre-crack approximately 2.5 ± 0.5 mm in length. An illustration of the CELS sample tested is shown in Fig. 3.

2.2.2. Pre-cracking and geometric details for ENF

Three-point bending ENF tests were performed to compare the pure mode II results with those of the CELS specimens, taking into account any variation that may arise from differences in test set-up. Similar to the CELS specimens, two batches of ENF specimens were

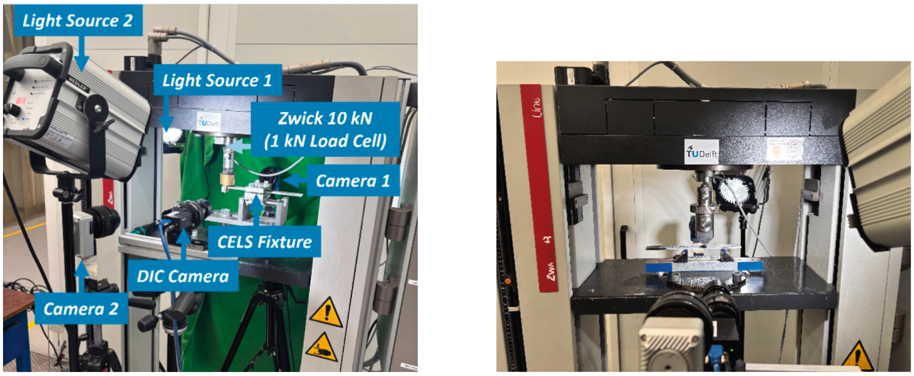

(a) (b)

Fig. 2. Experimental test set-up for pure Mode II in-plane shear test (a) CELS (b) ENF.

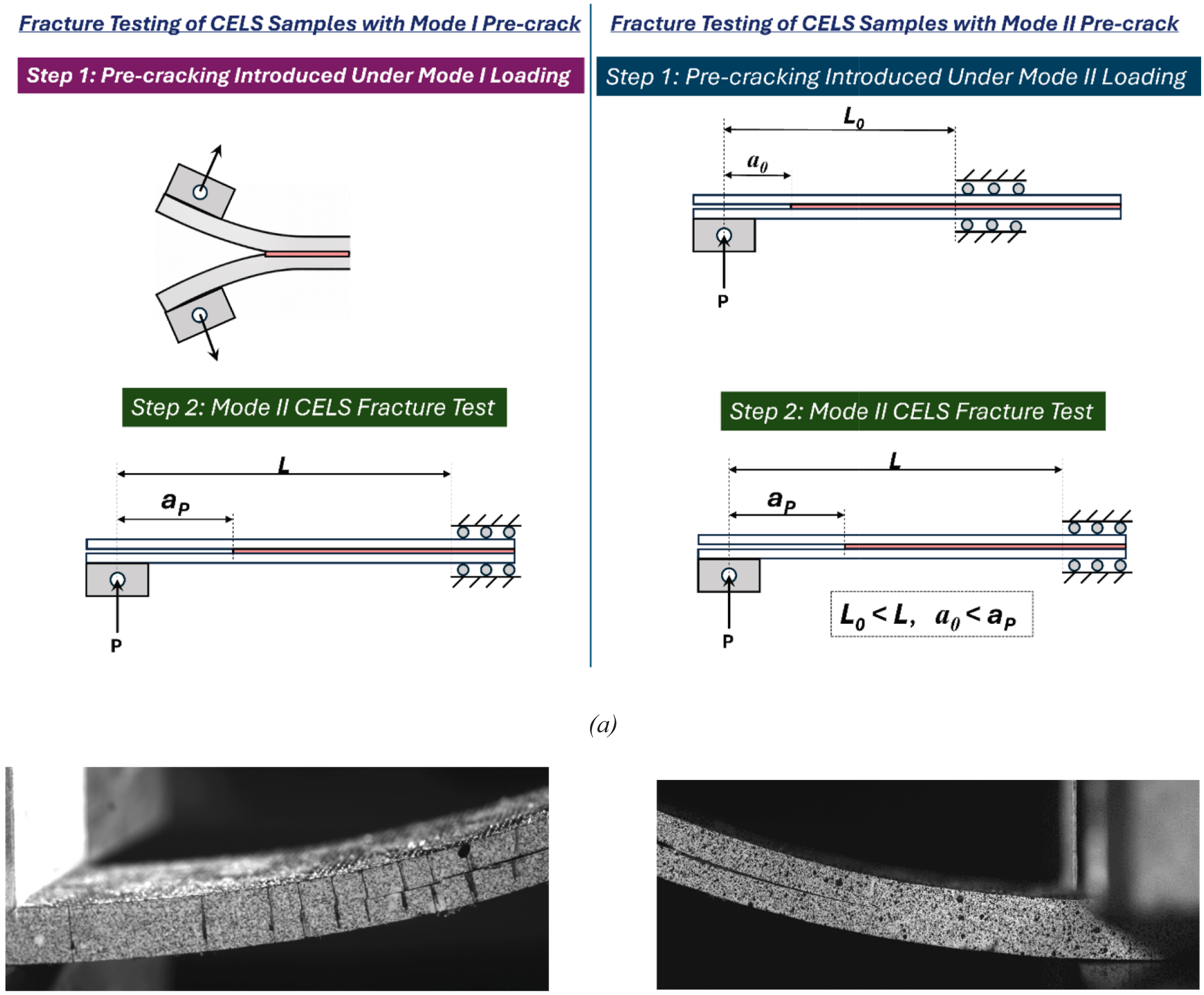

(a)

(a)

(c)

Fig. 3. (a) Schematic representation of pre-crack introduction and subsequent Mode II CELS testing: (Left) Mode I pre-cracking followed by Mode II testing, and (Right) Mode II pre-cracking followed by Mode II testing (Figure not to scale) (b) Rear-view camera image used for monitoring and measuring crack length in CELS specimen 1 (c) Digital Image Correlation (DIC) image of CELS specimen 1 showing the random speckle pattern applied for full-field strain analysis.

prepared with pre-cracks introduced under Mode I and Mode II loading conditions. The length of the pre-crack was maintained between 2.5 ± 0.5 mm [41,42]. The initial crack length introduced by the Teflon insert was 70 mm. It should be noted that all ENF specimens, irrespective of pre-cracking method, were tested under Mode II loading conditions at a displacement rate of 0.5 mm/min. Unloading at 5 mm/min was performed after failure.

The span length between the two bottom rollers was set to *“$2L = 100$ mm”*, in accordance with ASTM D7905 [10], with a distance of 50 mm maintained between the consecutive rollers. The initial crack length, a_0, measured from the first bottom roller to the crack tip, was approximately 30 ± 1 mm. For further clarity, please refer to Fig. 4.

3. Data reduction schemes

This section briefly outlines the different data reduction schemes used for the CELS and ENF tests. These data reduction schemes relied upon measurement of Load (P), displacement (δ), width of specimen (B), thickness of each arm (h), free length (L), and sometimes crack length (a). It is therefore essential to clearly outline each data reduction method, specifying the parameters it depends on, to facilitate accurate correlation and comparison of the results in subsequent discussions. Additional details of the data reduction schemes are given in the Appendix section.

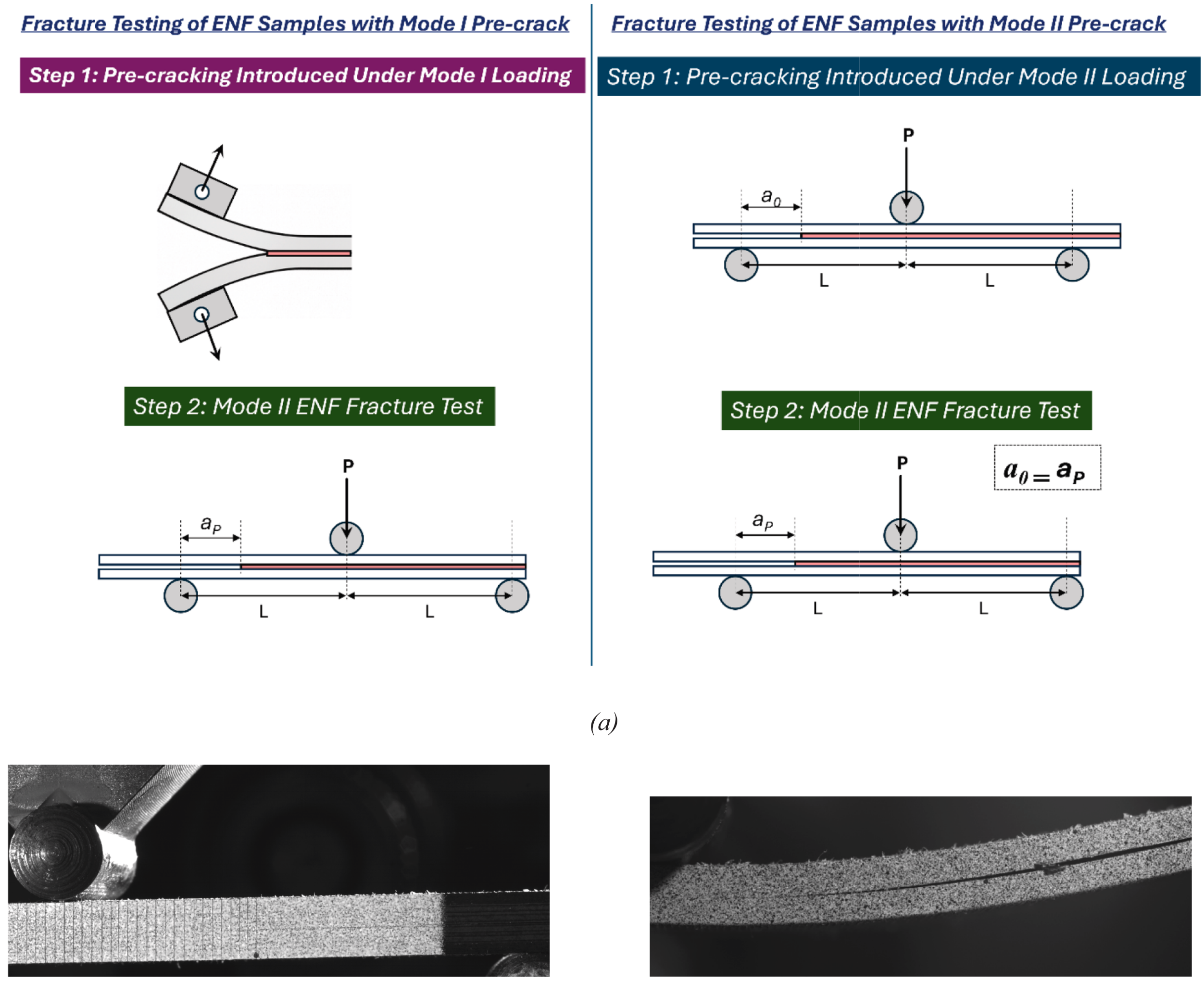

(a)

(b)

(c)

Fig. 4. (a) Schematic representation of pre-crack introduction and subsequent Mode II ENF testing: (Left) Mode I pre-cracking followed by Mode II testing, and (Right) Mode II pre-cracking followed by Mode II testing (Figure not to scale) (b) Rear-view camera image used for monitoring and measuring crack length in ENF specimen 1 (c) Digital Image Correlation (DIC) image of ENF specimen 1 showing the random speckle pattern applied for full-field strain analysis.

3.1. CELS

3.1.1. Simple Beam Theory (SBT)

The simple beam theory uses the Irwin-Kies equation (Appendix) to calculate the strain energy release rate in mode II.

$$G_{IIC} = \frac{9P^2a^2}{4B^2h^3E_f} \tag{1}$$

It should be noted that this equation is applicable only for specimens with a very thin bond layer, and where the flexural modulus of the adherend is significantly higher than the Young's modulus of the adhesive [11,15,22].

3.1.2. Corrected Beam Theory (CBT)

Corrected beam theory is a modification to SBT that utilizes a correction factor to measure crack length "a" and free length "L" [21,22]. Additionally, it accounts for the large deflection via the correction factor "F", includes a correction term for crack length in mode II "Δ_{II}", and also accounts for the bonded end-block by the factor "N" (Appendix A). The final expression for G_{IIC} using CBT is displayed by Eq. (2),

$$G_{IIC} = \frac{9P^2(a+\Delta_{II})^2}{4B^2h^3E_f}.F \tag{2}$$

3.1.3. Experimental compliance method (ECM)

The experimental compliance method [11] directly relates the measured crack length “a” to the observed compliance “C” in a cubic relationship as shown in Eq. (3),

$$C = C_0 + ma^3 \tag{3}$$

The values of “C_0” and “m” are constants, which are obtained by performing linear regression of the obtained values [11]. The final expression using ECM is given in Eq. (4),

$$G_{IIC} = \frac{3P^2a^2m}{2B} \tag{4}$$

3.1.4. Corrected Beam Theory with effective crack length (CBTE)

The data reduction schemes outlined above are often referred to as classical data reduction schemes. They rely heavily on the accurate measurement of crack length, which is highly sensitive to experimental errors. Moreover, the FPZs, which are significantly large in pure mode II loading, are only marginally captured using the conventional SBT or CBT methods. To address these limitations, an alternative approach was adopted, namely Corrected Beam Theory with Effective crack length (CBTE) [15,22]. This method employs the calculation of an effective crack length “a_e” to more accurately determine G_{IIC} (Appendix). However, a preliminary bending test is mandatory to estimate the flexural modulus of the samples. The strain energy release rate, as defined using CBTE, can be expressed as Eq. (5).

$$G_{IIC} = \frac{9P^2a_e^2}{4B^2h^3E_f} \times F \tag{5}$$

3.1.5. Compliance-Based Beam method (CBBM)

The compliance-based beam method (CBBM) also utilizes the apparent crack length “a_f” for calculating SERR in mode II [23,25]. The CBBM differs from the CBTE in that it uses apparent modulus instead of flexural modulus to calculate G_{IIC}. Moreover, CBBM assumes that the crack tip near FPZ is influenced by plasticity and micro-straining.

In the presence of a significant FPZ, the measured fracture toughness should be interpreted as an apparent or effective value, which incorporates both elastic and inelastic dissipation mechanisms. Equivalent or apparent crack length approaches (e.g., CBTE and CBBM) account for this by embedding the nonlinear FPZ contribution into an effective elastic crack length, thereby enabling the use of LEFM-based formulations without direct crack length measurement [15,23,24].

The apparent modulus is calculated using the initial compliance (C_{0C}) of the specimen, as determined in the tests (Refer to Appendix). The following equation highlights G_{IIC} as proposed by De Moura for CBBM [23,25].

$$G_{IIC} = \frac{9P^2a_f^2C_{0C}}{2B\left(3a_0^3 + L^3\right)} \times F \tag{6}$$

3.2. ENF

3.2.1. Direct Beam Theory (DBT)

The value of G_{IIC} for the ENF specimen using DBT can be expressed as [23,25]:

$$G_{IIC} = \frac{9P\delta a^2}{2B\left(2L^3 + 3a^3\right)} \tag{7}$$

During the testing of the ENF specimens, the large-displacement factor “F” was found to be significantly lower; therefore, it is ignored in the ENF calculation. Additionally, DBT does not require the calculation of the flexural modulus for the samples (Refer to Appendix).

While a separate numerical sensitivity study was not conducted in this work, the assumption of negligible friction is justified by the analytical framework established by Carlsson et al. [17]. According to their study, the reduction in the strain energy release rate due to friction can be quantified by the non-dimensional parameter:

$\frac{G_{IIC}(\mu)}{G_{IIC}} = 1 - \mu\left[\frac{4}{3}\left(\frac{h}{a}\right)\right]$(7(i)).

Where μ is the coefficient of friction, h is the adherend thickness, and a is the crack length. In our study, using the nominal values h $\approx$ 2.16 mm and $a_0 \approx$ 30 mm, even a conservative friction coefficient of $\mu = 0.05$ results in a very small dispersion of less than 1%. Furthermore, as Carlsson et al. [17] concluded, for standard ENF geometries with optimized a_0/L ratios, the contribution of frictional work to the overall energy balance is minimal. Given that our experimental G_{IIC} values for the toughened AF163-2 K adhesive were significantly higher (Refer to section 4) than these minor frictional losses, the assumption is physically and mathematically sound.

3.2.2. Compliance Calibration method (CCM)

The CCM method for the ENF specimens is similar to the ECM method for the CELS. The CCM requires a cubic relation between the measured crack length “a” and the compliance “C” of the specimen. Eqs. (3) and (4) can then be used for the CCM approach to calculate SERR for ENF specimens.

3.2.2. Corrected Beam Theory with effective crack length (CBTE)

The CBTE, as proposed by Blackman et al. s

$$G_{IIC} = \frac{9P^2 a_e^2}{16B^2 h^3 E_f} \tag{8}$$

3.2.3. Compliance-Based Beam method (CBBM)

The CBBM method proposed by De Moura [23,24] can be modified for the ENF specimen, similar to the CBTE method, as:

$$G_{IIC} = \frac{9P^2 a_f^2 C_{0c}}{2B\left(3a_0^3 + 2L^3\right)} \tag{9}$$

4. Results and discussion

The experimental analysis of CELS and ENF specimens was performed using data synchronized between the Zwick machine, DIC, and the other cameras. The raw data were post-processed using different data reduction schemes, giving the relation between fracture toughness, crack length, compliance, and the nature of the R-curve. The obtained data from the current analysis were then used as input in the numerical simulations to validate the experimental findings. The study's outcomes are summarized, forming the basis for subsequent discussion.

1.1. CELS

The test of the CELS sample, as per ISO 15114, began with measuring the compliance of the CELS specimen using the inverse ELS test. A linear regression was performed after using a cube root relation between compliance and free length to obtain the clamp correction factor (Δ) and flexural modulus (E_f) (see Fig. 5). The measured E_f and $|\Delta|$ of the specimen are $\approx$ 147910 MPa and 11.09 mm, respectively.

4.1.1. Mode I Pre-Crack – CELS

Mode I pre-cracking in the CELS specimen was restricted to 2–3 mm (the reader is referred for pre-cracking details to Section 2.2.1). The initial crack length was recorded for each sample, and then the specimens were subjected to in-plane shear loading using the CELS fixture. After reaching the peak load, when the force began to increase again under the clamping pressure, the sample was unloaded. A stable cohesive failure was observed in the bond layer. The force–displacement diagram for Mode I pre-crack specimens is shown in Fig. 6a. The measured peak load for the specimens was 893 ± 33.36 N, with a standard deviation of 3.73%. The variation in the peak load and the displacement assures that there was minimal variation in the initial pre-crack. However, the measured displacement for all the samples was relatively high, which can be attributed to the specimen's overall thickness (Fig. 6). Hence, it was imperative to

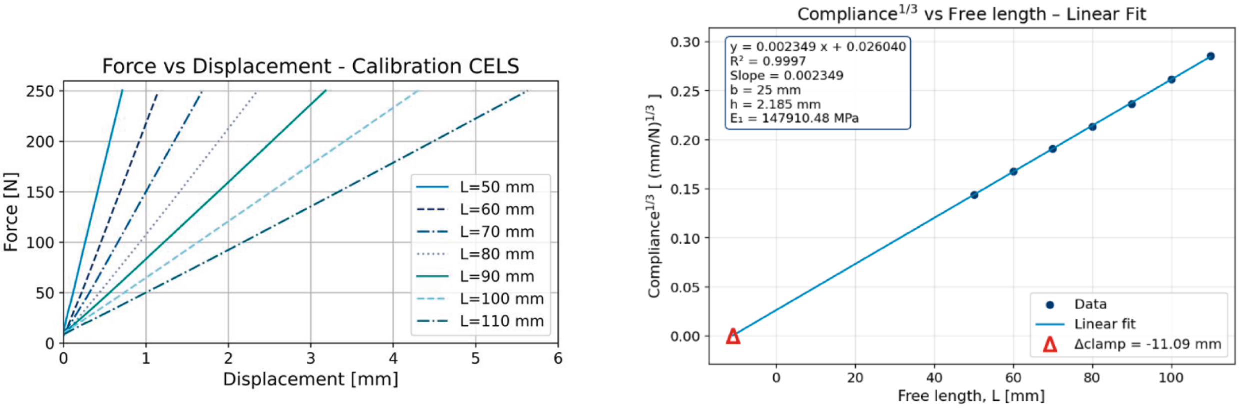

(a) (b)

Fig. 5. (a) Compliance Calibration performed on inverse CLS configuration at different free lengths to obtain flexural modulus, (b) Flexural modulus and clamp correction factor obtained by performing linear regression analysis.

account for the significant displacement correction factor “*F*” in the different data reduction schemes. The end-load block correction factor “*N*” was negligible; hence, it was ignored in the calculations. The decision to neglect the end-load block correction factor *N* is supported by both a sensitivity assessment and evidence from the literature. In the present study, a preliminary evaluation indicated that the contribution of *N* to the apparent crack length and, consequently, to the calculated G_{IIC} values was approximately 1% or less, which falls within the typical experimental scatter observed in Mode II fracture tests. Therefore, its influence on the final results is negligible.

This assumption is consistent with previous studies. For example, De Moura [23] shows that simplified correction procedures associated with load-block and geometric factors introduce errors typically below 0.1%, indicating minimal impact on fracture toughness evaluation. Furthermore, round-robin studies conducted during the development of the ISO 15114 [11] standard (as summarized in the literature) have shown that these correction factors are generally small and can be safely neglected under standard test conditions.

In light of these observations, neglecting *N* in the present analysis is justified and does not affect the accuracy of the reported G_{IIC} values.

The classical data reduction schemes that utilize the observed crack length “*a*” were employed to calculate G_{IIC} and get the R-curve (Fig. 6c). It should be noted that the physical crack length *(a)* and the equivalent or apparent crack length are treated as distinct parameters in the analysis. The equivalent crack length *(a_e)* and apparent crack length *(a_f)* are derived from compliance-based methods (CBTE and CBBM) and implicitly account for the contribution of the fracture process zone, whereas the physical crack length *(a)* corresponds to the visually measured crack front. The images from the DIC camera and camera 1 were carefully correlated to measure the crack length (Fig. 2a).

The curve displayed a steady growth with a plateau region before the crack reached the clamp (Fig. 6c). However, a significant difference was observed in the G_{IIC} value between the ECM and the SBT or CBT methods. The measured G_{IIC} value using the ECM method was 17.3 ± 1.19 N/mm, whereas the SBT method yielded a significantly lower G_{IIC} value of 10.13 ± 0.87 N/mm. The CBT

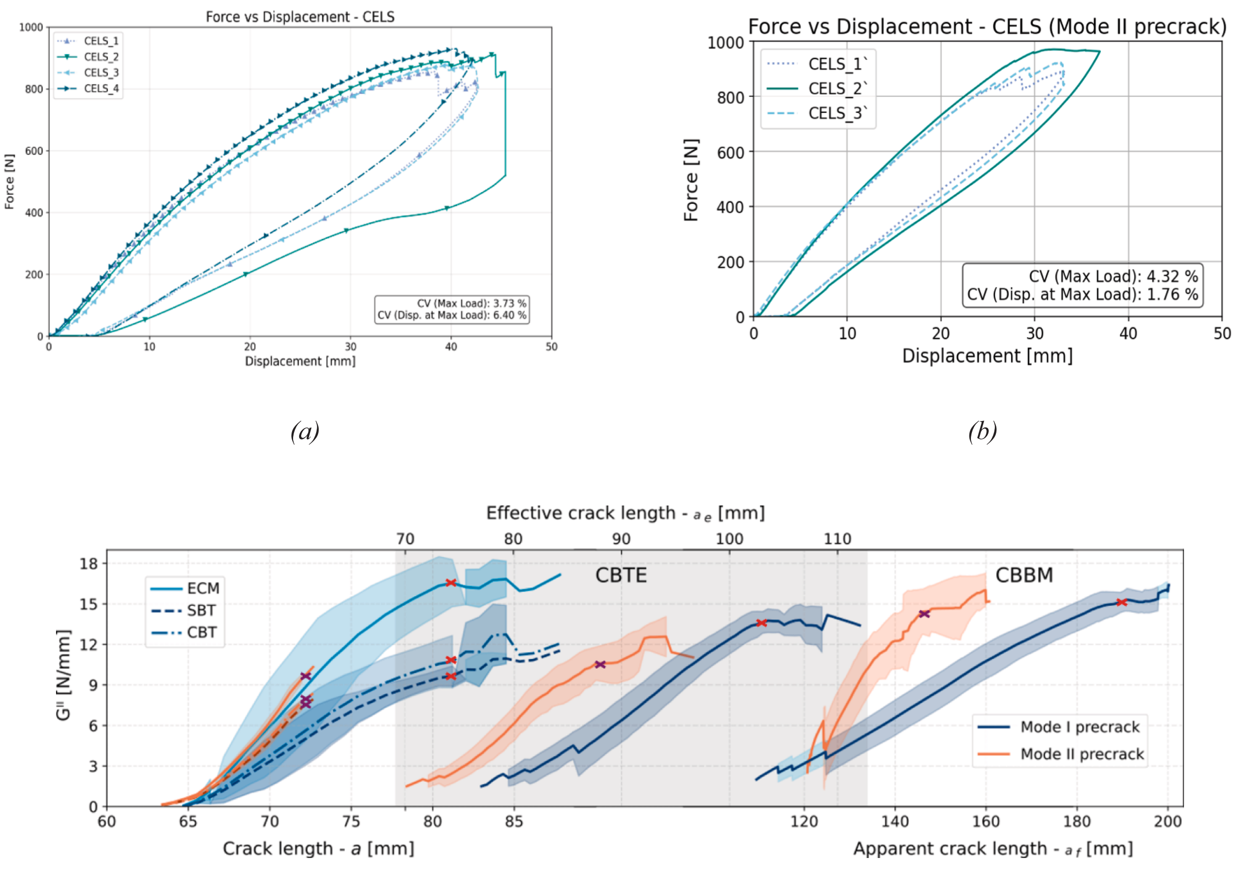

(a) *(b)*

(c)

Fig. 6. (a) Force Displacement curve for mode I pre-cracked specimens showing a good repeatability in the experiment. (b) Large displacement for the CELS specimen, for which factor “F” is utilized in the data reduction schemes. (c) R-curve developed using various data reduction schemes. G_{II} varies according to physical (a), effective (a_e), or apparent crack length (a_f), depending on the method used. They are treated as distinct parameters in the analysis. The bold line represents the mean value, while the shaded area represents the standard deviation.

method, which uses a correction factor for crack length and clamped length in the SBT method, yielded a value of 11.26 ± 1.85 N/mm. The difference of ≈70% between the ECM and SBT results can be attributed to the ECM method's strong dependence on specimen compliance, which tends to be substantially higher for thinner specimens.

The CBTE and CBBM methods were also employed because significant discrepancies were observed in the results obtained from classical data reduction schemes. The R-curves exhibited by CBTE and CBBM show a steady rising progression followed by a distinct plateau region (Fig. 6c). This plateau value corresponds to the steady state of crack propagation, aligning near the maximum load, compensating for the parasitic effects of the clamped region. The G_{IIC} value for CBTE was 13.6 ± 0.84 N/mm, whereas for CBBM, it was comparatively higher, at 15.27 ± 0.66 N/mm. Previous studies have shown that fracture toughness values obtained using effective crack length methods are in agreement with those derived from J-integral approaches, confirming the validity of energy equivalence even in the presence of significant nonlinear deformation [26,49]. Hence, the reported G_{IIC} values should be interpreted as effective fracture energies that reflect both crack-tip and process-zone dissipation mechanisms.

A notable distinction between the two methods was observed in the corresponding apparent crack lengths: the "a_f" value obtained from the CBBM method extended beyond the clamped region and was significantly higher than that from CBTE. In contrast, the "a_e"

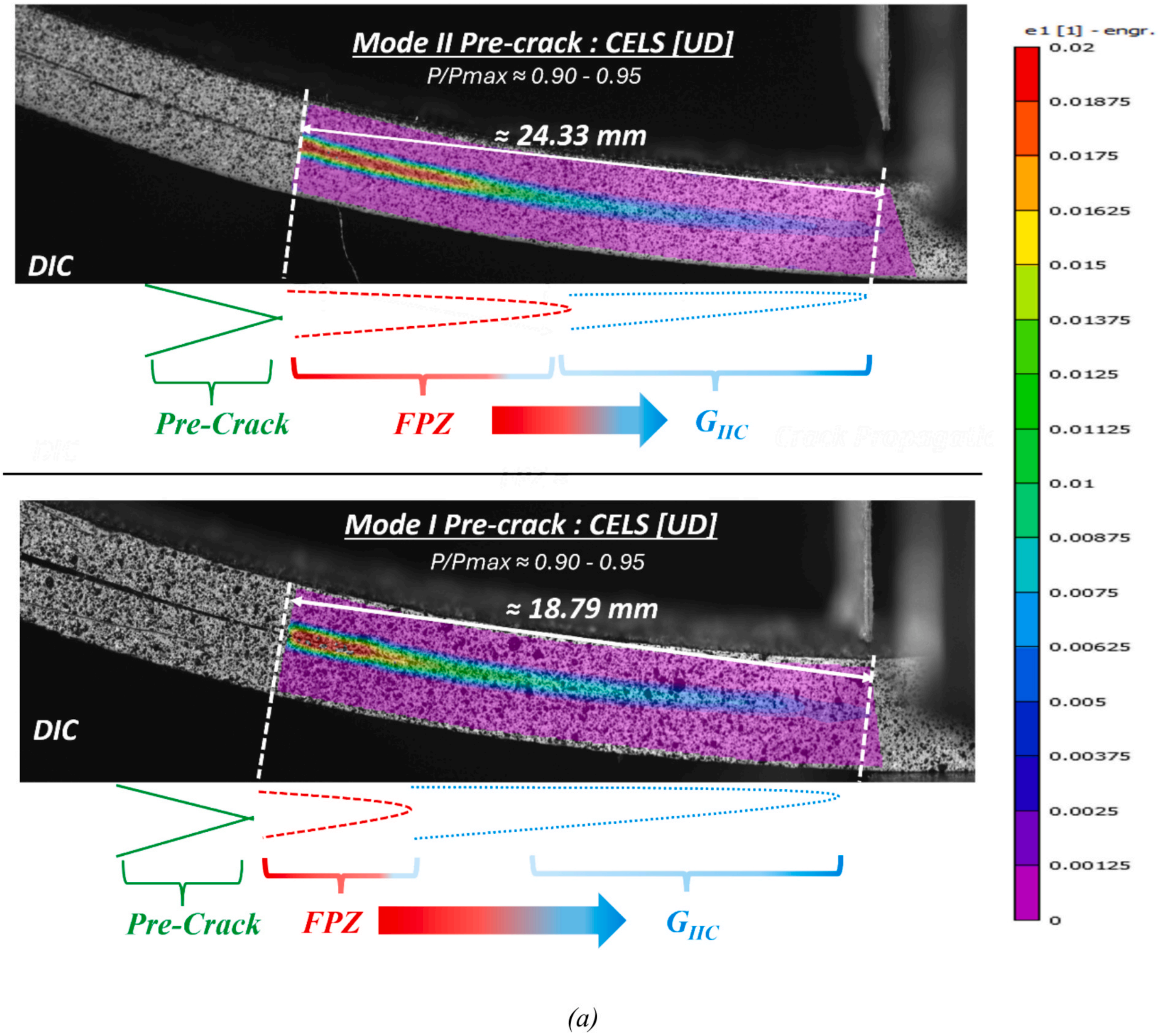

Fig. 7. (a) DIC-derived major principal strain component (e1 [1]) along the bond-line direction illustrating the evolution of the FPZ ahead of the crack tip for Mode I and Mode II pre-cracked CELS specimens for qualitative comparison of FPZ evolution. The observed differences in G_{IIC} are associated with variations in FPZ development resulting from the pre-cracking mode. Images are captured at approximately 90–95% of the critical load to compare the FPZ development at a near-critical state (b) Annotated fracture surfaces of CELS specimens showing crack evolution for specimens pre-cracked under (top) Mode II and (bottom) Mode I pre-cracked conditions. The initial insert region (a_0), pre-cracked zone (a_P), and steady-state Mode II propagation are identified. The crack growth direction is indicated, highlighting differences in fracture process development associated with the pre-cracking mode. (not to scale).

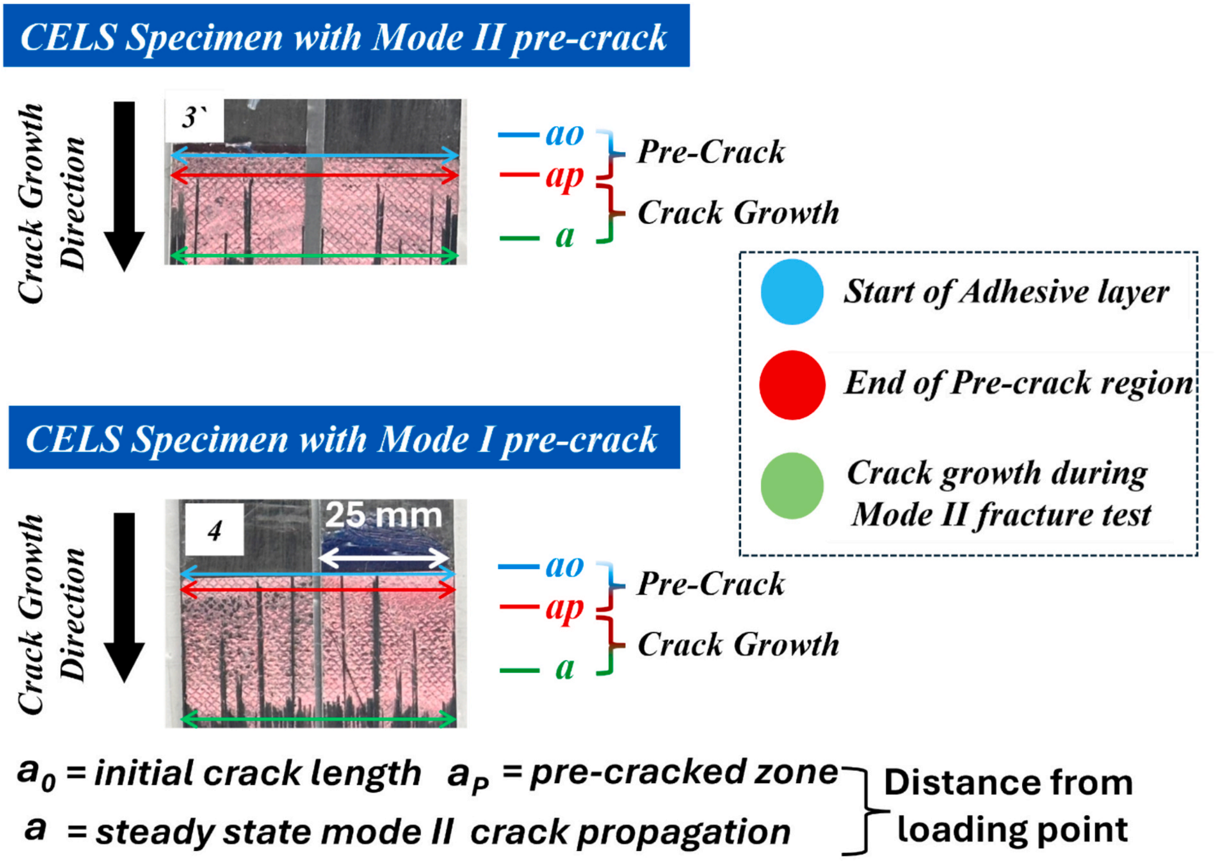

(b)

Fig. 7. (*continued*).

value for CBTE remained within the clamping region. This variation arises from the definition of the flexural modulus used in each formulation. The CBTE method utilizes the experimentally measured flexural modulus (E_f), which is determined from the non-pre-cracked side of the specimen and accounts for the experimentally obtained clamp correction factor (Δ). In contrast, the CBBM method uses the apparent flexural modulus (E_{1f}), derived from the initial compliance of the pre-cracked configuration and the absence of the “Δ” term in its formulation.

The use of E_{1f} inherently accounts for additional deformation near the crack tip and nonlinear compliance effects not captured when using E_f [23,24]. This difference introduces a compliance mismatch and energy dissipation ahead of the crack tip, contributing to scatter in the results.

4.1.2. Mode II pre-crack – CELS

The Mode II pre-crack for the other CELS specimens was provided by loading the specimen with a shorter free length of about 65 mm, such that the ratio between the initial crack and the free length is “$a_0/L = 0.8$” to get stable crack initiation (details of the pre-cracking procedure are discussed in section 2.2.1). The loading was immediately terminated once a displacement of the initial crack line markers was observed, indicating the initiation of the crack. Although the ISO 15114 standard recommends Mode II pre-cracking, its use in the literature is relatively limited due to concerns regarding potential stable crack growth during the pre-cracking process [39]. The pre-crack length was carefully controlled within the range of 2–3 mm to ensure sufficient remaining length for complete crack propagation and to allow the R-curve to reach a distinct plateau. For the pre-cracked fracture test, a longer free length of 95 mm was chosen to allow the crack to grow completely, such that the ratio of a_p/L is maintained at 0.65.

The pre-crack fracture test encouragingly displayed a stable disbond growth with a cohesive failure in the bond layer. The observed failure load for the pre-crack test was 934 ± 31.6 N, which is 4.5% higher than the fracture test using a mode I pre-crack. The initial portions of the load–displacement curves for both pre-cracking modes were similar; however, the nonlinear regime revealed a pronounced difference. The mode I pre-cracked CELS tests exhibited greater plastic deformation before failure, resulting in a displacement-to-failure ratio nearly 35% higher than that of the mode II pre-cracked CELS tests.

This variation can arise from the distinct FPZ formed ahead of the crack tip, depending on the pre-cracking mode (Fig. 7a). The DIC-derived strain contours shown in Fig. 7a and 9a represent the major principal strain component (*e1* [1]), evaluated along the bond-line direction. This strain component was selected as it provides a consistent measure of deformation ahead of the crack tip. The spatial distribution and gradient of *e1* [1] are used to qualitatively identify the extent and evolution of the FPZ. It is observed that specimens pre-cracked under Mode II loading exhibit a more extended FPZ compared to those pre-cracked under Mode I conditions. This difference reflects the influence of the initial crack tip condition on subsequent damage evolution under Mode II loading.

To further quantify this behavior, various data-reduction schemes were employed to construct the R-curve for Mode II pre-cracked CELS tests. The classical data reduction schemes, ECM, SBT, and CBT, showed a steady nature of the R-curve (Fig. 6c). The G_{IIC} value for ECM, SBT, and CBT is 10.34 ± 0.3, 8.01 ± 0.17, and 8.45 ± 0.18 N/mm, respectively. These results demonstrated significantly less scatter compared to those obtained from Mode I pre-cracked CELS tests; however, an apparent plateau in the R-curve was not observed.

This can be attributed to the extensive FPZ formed ahead of the crack tip in Mode II pre-cracked CELS specimens, which obscures

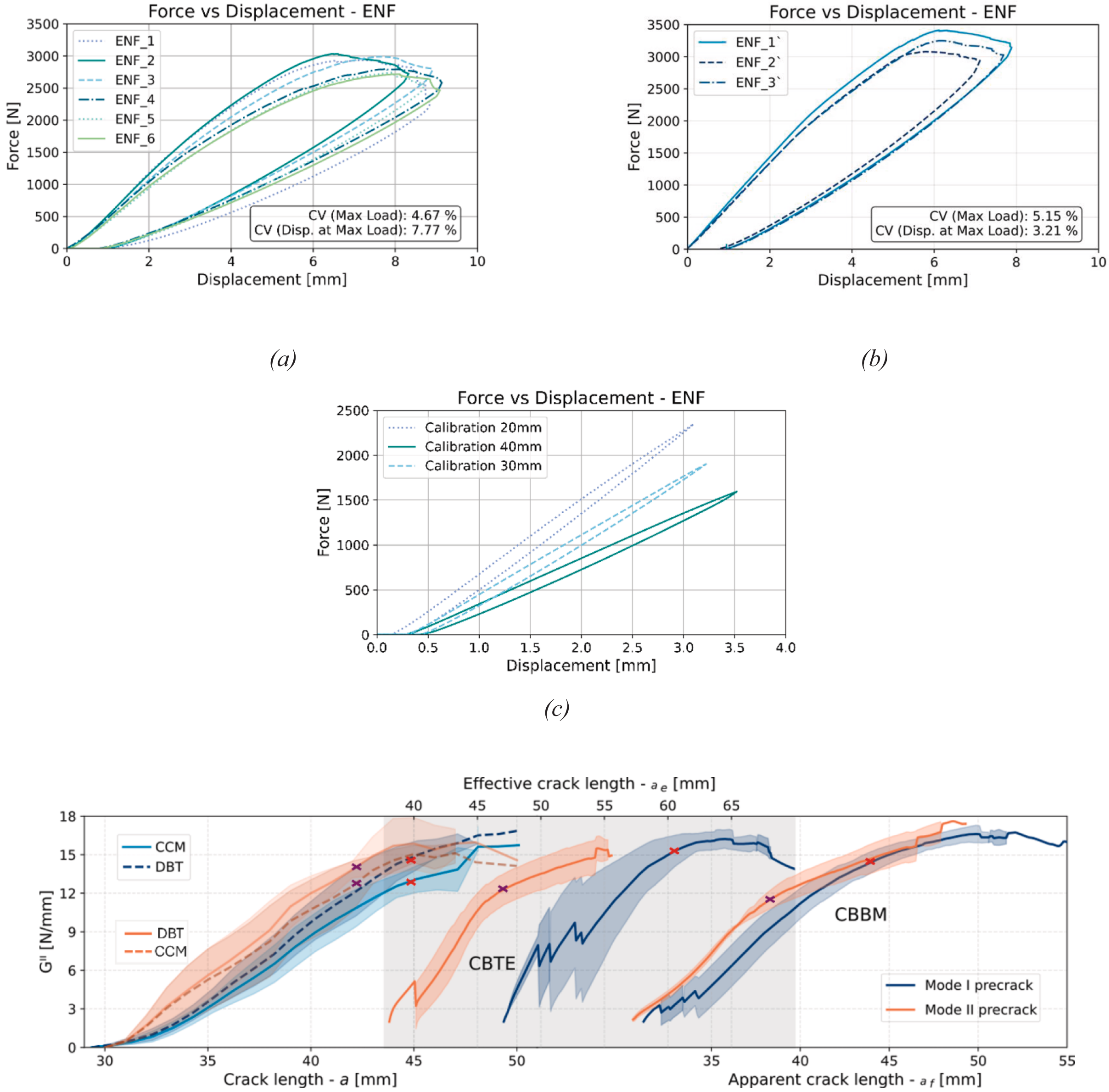

(a)

(b)

(c)

(d)

Fig. 8. (a) Force-displacement diagram for the mode I pre-cracked ENF specimens, (b) Force-displacement diagram for the mode II pre-cracked ENF specimens, (c) Compliance Calibration performed for the ENF specimens, (d) R-curve developed using various data reduction schemes. G_{II} varies according to physical (a), effective (a_e), apparent crack length (a_f), depending on the method used. They are distinct parameters in the analysis.

precise crack tip tracking and complicates the accurate estimation of energy release rates. Consequently, the CBTE and CBBM approaches, which are based on apparent crack lengths, were adopted. The R-curves developed using CBTE and CBBM clearly exhibited a plateau region. The G_{IIC} value, obtained using the CBTE method, was 11.2 ± 0.93 N/mm (Fig. 6c), whereas the CBBM value was 14.1 ± 1.1 N/mm (Fig. 10c). Notably, the value of apparent crack length (a_e *or* a_f, using the CBTE and CBBM methods) was significantly lower than that of the mode I pre-cracked CELS test. The values of G_{IIC} and apparent crack length for CBTE were consistently lower than those of CBBM, as discussed in Section 4.1.1.

The analysis of CBTE or CBBM methods indicates that the apparent crack length (a_e *or* a_f) is much higher than the observed crack length (a) (see Fig. 6c). This clearly indicates that in mode II pre-crack CELS tests, the results show the formation of a large FPZ extending beyond the free length ($L = 95\ mm$) into the clamped region (see Fig. 6c). The visual observation from the disbonded surface in mode I and mode II pre-crack CELS specimens confirms the difference in crack growth (Fig. 7b, A1).

It is important to highlight that after the final failure, the specimens were opened in mode I using manual force to see the fracture surface, as continuing the test in Mode II can damage the specimen due to high bending forces. Consequently, apparent crack length–based approaches, such as CBTE and CBBM, provide a more reliable estimation of G_{IIC} under these conditions. Additionally, mode II pre-crack CELS tests yield a lower value of G_{IIC} than mode I pre-crack CELS tests, regardless of the data reduction schemes employed.

This difference can be attributed to the nature of FPZs created ahead of the crack tip. Mode I pre-cracking forms a localized FPZ, which subsequently evolves into a shear-dominant FPZ for G_{IIC}, evaluated during actual test, whereas a shear-driven FPZ is already present in Mode II pre-cracked specimens. Mode I pre-cracking generates a sharp, singular crack tip with a negligible initial shear-damage zone. Upon transitioning to Mode II loading, this configuration requires significant energy to initiate plastic deformation and develop a new, shear-dominant FPZ, leading to higher G_{IIC} values (Fig. 7a). On the contrary, mode II pre-crack CELS specimens induce a broader FPZ that distributes damage ahead of the crack tip, thereby reducing the localized energy release rate at the crack tip and yielding a lower fracture toughness estimate.

1.2. *Three-point bending ENF*

4.2.1. *Mode I pre-crack − ENF*

All the ENF specimens exhibited stable crack growth, displaying cohesive failure in the bond layer. The force–displacement curve of the ENF specimens is shown in Fig. 8. The peak load exhibited excellent repeatability, with an average value of 2868 ± 134 N in Mode I pre-cracked ENF specimens. The mode II pre-cracked ENF specimens displayed a peak load of 3240.66 ± 161.2 N. The displacement at the maximum failure load was also significantly lower in the ENF specimens compared to the CELS specimens, exhibiting a more global stiff response and reduced compliance effects. The nonlinear portion of the load–displacement curve showed pronounced plasticity, similar to the response observed in the Mode I pre-cracked CELS specimens. This behavior reinforces that Mode I pre-cracking produces a relatively smaller FPZ ahead of the crack tip, which in turn promotes localized plastic deformation during the final fracture stage.

The critical Mode II strain energy release rate (G_{IIC}) for Mode II ENF tests was evaluated at the peak force to avoid the parasitic effects of local compression and constraints from the loading indenter, a standard protocol in literature to ensure data integrity [28,50,55–58]. The classical data reduction schemes DBT and CBT were used to develop the R-curve. The DBT and CCM showed a stable nature of the R-curve with an apparent plateau. The obtained G_{IIC} values using the DBT and CCM methods are 14.71 ± 1.08 and 13.09 ± 1.22 N/mm, respectively. The relatively low scatter in G_{IIC} values compared to Mode I pre-cracked CELS specimens highlights the lower compliance sensitivity of the ENF configuration (Fig. 6c and 8d).

The CBTE and CBBM methods are used to further investigate the effect of compliance. The extracted G_{IIC} value for CBTE and CBBM is 15.38 ± 1.03 and 14.67 ± 0.99 N/mm, respectively. The scatter in CBTE and CBBM G_{IIC} values in the mode I pre-cracked ENF specimens is significantly lower than that of mode I pre-cracked CELS samples. This behavior can be attributed to the CELS configuration's greater sensitivity to compliance variations, which increases scatter in the evaluated G_{IIC} values.

4.2.2. *Mode II pre-crack – ENF*

The G_{IIC} for mode II pre-cracked ENF specimens using CBTE and CBBM are 12.34 ± 1.08 N/mm and 11.85 ± 0.87 N/mm (Fig. 8d). The classical data reduction schemes DBT and CCM yielded G_{IIC} of 14.33 ± 1.7 N/mm and 13.06 ± 1.62 N/mm. The Mode II pre-cracked ENF specimens exhibited trends consistent with Mode II pre-cracked CELS specimens, showing lower strain-energy-release-rate values across most methods. The slightly higher G_{IIC} estimates from the CBTE method in ENF tests, compared to CELS, can be attributed to the different correction methodologies: CELS utilizes an experimentally derived clamp correction factor Δ, and the CBTE for ENF relies on an analytical compliance formulation that incorporates the effective bending modulus and shear strength (G_{13}) of the laminae to determine the apparent crack length (see Appendix for formulation) [11,23,59]. Notably, the CBBM results for the mode II pre-crack ENF configuration showed the strongest consistency with the mode II pre-crack CELS data. This is because CBBM accounts for individual specimen compliance, stress concentration near the crack-tip and utilizes an equivalent crack length, effectively mirroring the flexural modulus and clamp correction effects provided by the CBTE method in CELS setups. Consequently, the data support the use of CBBM as a robust alternative for ENF characterization when high compliance and pre-existing damage zones are present.

These findings reinforce the capability of apparent-crack-length-based methods to accurately determine G_{IIC}, even when test configurations are highly sensitive to compliance. This contrast becomes more evident when compared to CELS specimens, which, owing to their cantilever-based configuration, exhibit greater compliance and consequently discrepancies between apparent and flexural moduli. The ENF configuration, on the other hand, functions as a supported beam, resulting in lower compliance and more consistent stiffness characteristics. Therefore, the CBTE and CBBM methods for CELS and ENF configurations, respectively, demonstrate convergent reliability, even in the presence of fixture effects such as clamping constraints and roller friction, and a large FPZ ahead of the crack tip.

Importantly, mode I pre-cracking in CELS and ENF specimens displayed higher fracture toughness than mode II pre-cracking due to a smaller initial fracture process zone with a larger fracture process zone in the stage of fracture testing. Mode I pre-cracking exhibits a localized FPZ, which subsequently evolves into a shear-dominant FPZ for G_{IIC}, as observed during actual testing. In contrast, a shear-driven FPZ is already present in Mode II pre-cracked specimens (Fig. 7a and 9a). This pre-existing FPZ also influences the global stiffness response, allowing the displacement behavior to be captured accordingly. Mode II pre-cracking generates a broader and more diffuse FPZ, resulting in reduced strain energy release rate, which yields more conservative G_{IIC} values.

1.3. Computational study and analysis

The experimental observations were further studied through computational simulations designed to replicate the force–displacement response. All computational analyses were performed using Abaqus/CAE 2024 [60]. Two-dimensional plane-strain finite element (FE) models were developed to conduct the simulations and minimize computational cost [61,62]. The adherends were partitioned into individual prepreg layers, comprising a total of 16 plies, replicating the experimental configuration. A very thin delamination layer was introduced just above the first ply, adjacent to the interface, to monitor potential crack migration (see Fig. 10a).

The material properties of unidirectional (UD 0°) IM7/8552 and the resin used for delamination were obtained from the literature [63,64]. Each individual ply was properly assigned material orientation along the fiber direction. The properties employed for the CFRP in the numerical study are summarized in Tables 1 and 2. The adhesive bond layer (AF163-2 K) was modeled as a cohesive layer tied to the upper and lower adherends using a tie constraint. A bilinear cohesive traction–separation law was adopted to simulate the behavior of both the adhesive disbond and delamination layers [14,65]. The quadratic stress criterion (QUADS) was used to define the damage initiation traction behavior of the adhesive. A single layer of cohesive elements was employed through the adhesive thickness to represent its response. The cohesive elements were modeled with a finite physical thickness of 0.17 mm. These moduli (*E and G*) provide the correct physical stiffness of the bond line. This approach avoids the need for an arbitrary penalty stiffness and ensures the numerical model accurately reflects the experimental compliance. A mesh convergence study was carried out along the length to ensure numerical accuracy.

The three-point bending ENF configuration was modeled using three analytical rigid rollers to replicate the experimental fixture. The two bottom support rollers were fully constrained in all degrees of freedom (Encastre), while the top loading roller was constrained to move only in the vertical direction (y-axis). Loading was applied via a prescribed downward displacement to the top roller, consistent with the experimental displacement-controlled setup. The CELS specimen boundary conditions were defined to accurately mimic the clamped and supported ends of the fixture. The end block at the loading point was subjected to a vertical displacement (y-direction). At the opposite end, a roller support arrangement was implemented; this allowed for horizontal translation (x-direction) while constraining vertical movement, thereby replicating the kinematic behavior of the physical test assembly.

The mode I critical strain energy release rate (G_{IC}) of the adhesive was obtained from the DCB tests reported in Reference [66]. The simulations incorporated different G_{IIC} values obtained from experimental data reduction schemes, which exhibited a notable variation ranging from 8.01 ± 0.17 N/mm to 17.3 ± 1.19 N/mm. The geometry and boundary conditions applied in the numerical models accurately replicated the experimental setup.

The numerical simulations consistently reproduced stable cohesive failure within the adhesive layer, in complete agreement with the experimental failure patterns. The scalar stiffness degradation contour plots obtained from the simulations further substantiated these findings, demonstrating a progressive damage evolution pattern consistent with cohesive failure mechanisms observed experimentally (see Fig. 10b and c). A systematic parametric analysis revealed that higher G_{IIC} inputs led to increased failure loads and slight deviations in the post-yield region of the load–displacement response, confirming the direct sensitivity of global joint behavior to interfacial fracture energy.

Three G_{IIC} input values, 9, 11, and 13 N/mm, were examined to achieve the best correlation with experimental results (see Fig. 11). Among these, the $G_{IIC} = 11$ N/mm condition most accurately reproduced both the failure load and the global displacement response for the different CELS and ENF configurations. Furthermore, the plastic softening region in the simulated curves showed a close resemblance to the Mode II pre-cracked CELS and ENF response, indicating an identical FPZ. In the Mode I pre-cracked ENF specimens, the simulated displacement at peak load was slightly lower than the experimental mean. However, the magnitude of the peak load remained nearly identical. This indicates that the numerical model slightly overpredicted the specimen stiffness while maintaining accurate energy dissipation characteristics for Mode I pre-cracked fracture tests.

This finding highlights that the CBTE method for CELS and the CBBM method for ENF, used in the data extraction for Mode II pre-cracked samples, are displaying the best results. The spread of G_{IIC} was primarily attributed to the influence of pre-crack type (Mode I vs. Mode II) and specimen compliance effects inherent in different test configurations.

The G_{IIC} value, obtained using the CBTE and CBBM method, was 11.2 ± 0.93 N/mm and 11.85 ± 0.87 N/mm for the mode II pre-crack CELS and ENF tests, respectively, which accurately replicates the fracture characterization (Table 3).

5. Conclusions

This study developed a detailed understanding of the pure Mode II characterization of adhesively bonded joints, focusing on the effects of pre-cracking and compliance in various test configurations. Two different test configurations, the CELS and ENF tests, were

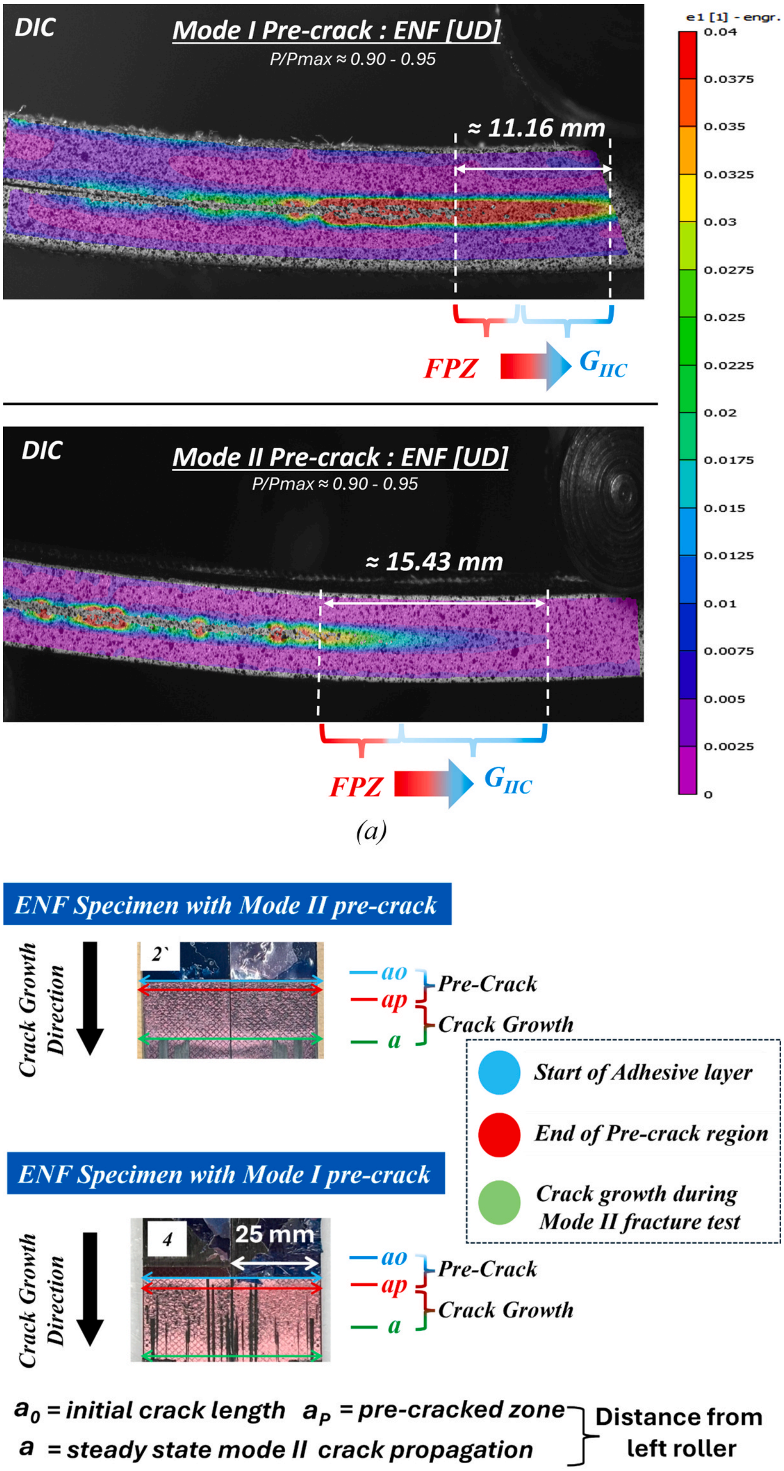

(a)

(b)

(caption on next page)

Fig. 9. (a) DIC-derived major principal strain component (e1 [1]) along the bond-line direction illustrating the evolution of the FPZ ahead of the crack tip for Mode I and Mode II pre-cracked ENF specimens for qualitative comparison of FPZ evolution. The observed differences in G_{IIC} are associated with variations in FPZ development resulting from the pre-cracking mode. Images are captured at approximately 90–95% of the critical load to compare the FPZ development at a near-critical state (b) Annotated fracture surfaces of ENF specimens showing crack evolution for specimens pre-cracked under (top) Mode II and (bottom) Mode I pre-cracked conditions. The initial insert region (a_0), pre-cracked zone (a_P), and steady-state Mode II propagation are identified. The crack growth direction is indicated, highlighting differences in fracture process development associated with the pre-cracking mode. (not to scale).

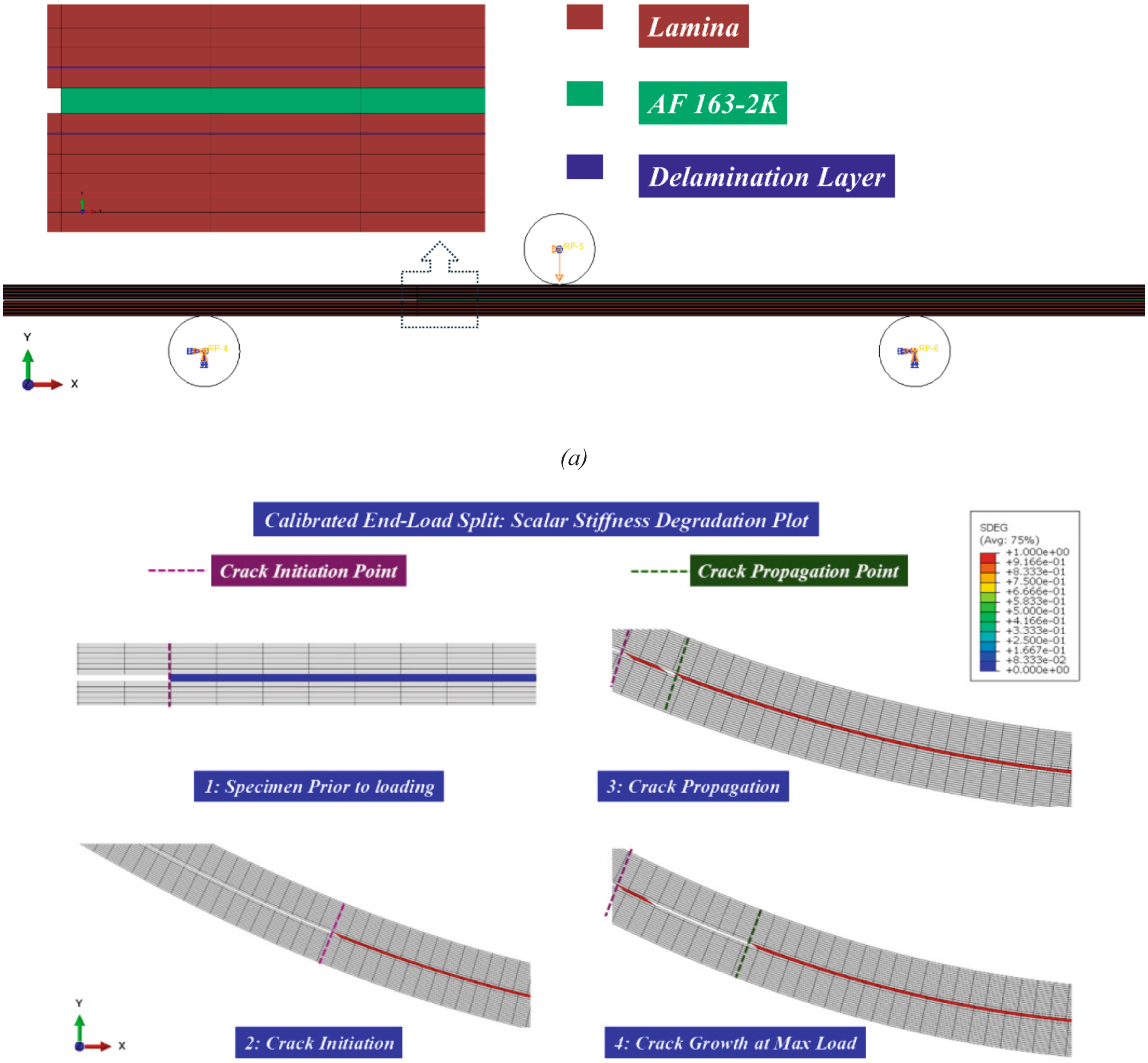

(a)

(b)

Fig. 10. (a) Schematic representation of ENF specimen (similar for CELS) modeled in Abaqus CAE 2024. The delamination layer is inserted above and below the plies adjacent to the interface to track crack migration Scalar Stiffness Degradation Plot showing progressive failure for (b) CELS (c) ENF.

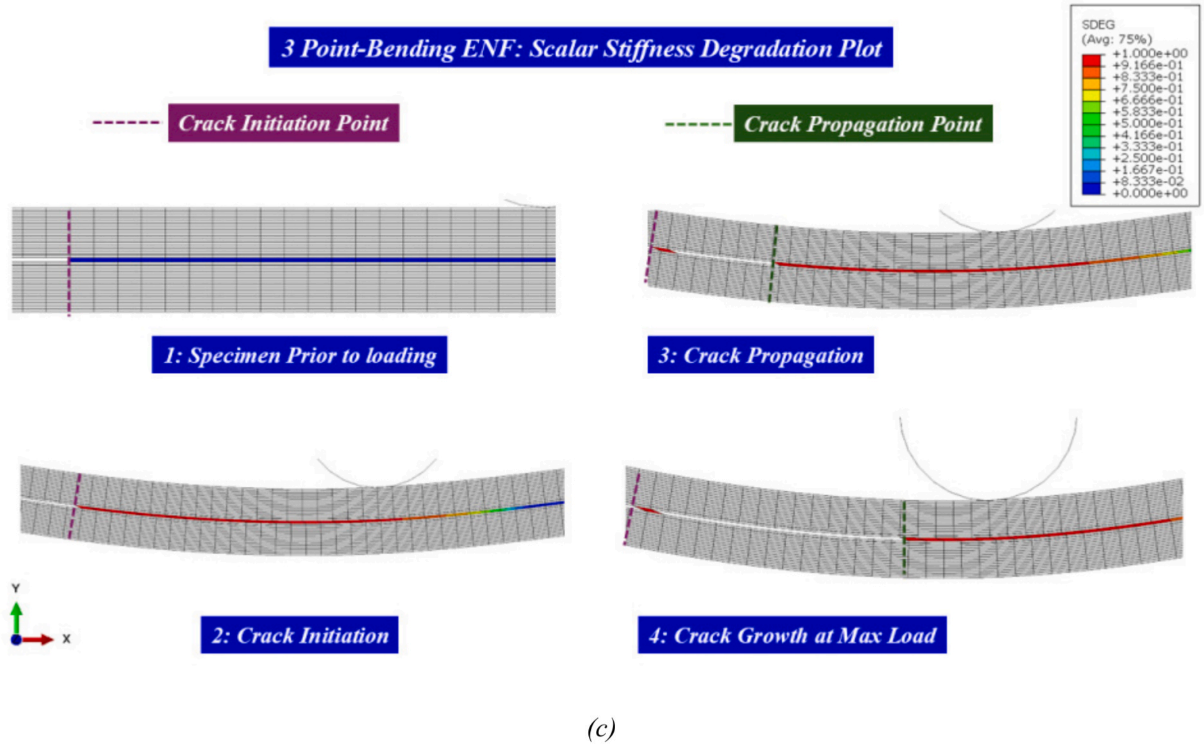

Fig. 10. (*continued*).

Table 1
Material properties of IM7/8552 [63,64].

E_{11} [MPa]	146,700
$E_{22} = E_{33}$ [MPa]	8700
$G_{12} = G_{13}$ [MPa]	5160
G_{23} [MPa]	3000
$\upsilon_{12} = \upsilon_{13}$	0.3
υ_{23}	0.4

Table 2
Cohesive element properties for IM7/8552 used in FE modeling [64].

G_{IC} [N/mm]	G_{IIC} [N/mm]	σ_n [MPa]	σ_t [MPa]
0.24	0.739	80.1	97.6

performed under quasi-static loading. The disbond growth in all specimens, despite pre-cracking and compliance effects, exhibited stable crack growth with cohesive failure in the adhesive. The lessons learned from this study are summarized below:

- Mode II CELS and ENF specimens, owing to their cantilever or 3-point bending configuration, exhibit differences in compliance and consequently discrepancies between G_{IIC}. A significant difference in the profile and magnitude of the R-curve was observed when using various data reduction schemes, including the classical and apparent crack length based data reduction schemes.
- The data reduction schemes displayed a significant variation in estimating G_{IIC} values, ranging from 8.07 ± 0.17 to 17.3 ± 1.19 N/mm, depending upon the modes of pre-crack and compliance effect. The classical data reduction schemes displayed greater sensitivity to measured crack length because of different FPZs. Additionally, these schemes were susceptible to compliance effects, particularly in cases involving highly deformable specimens or setups. The CBTE and CBBM methods for CELS and ENF configurations, respectively, demonstrate convergent reliability, even in the presence of fixture effects such as clamping constraints and roller friction, and a large FPZ ahead of the crack tip. The G_{IIC} value, obtained using the CBTE method, was 11.2 ± 0.93 N/mm for the mode II pre-crack CELS, and the G_{IIC} value of 11.85 ± 0.87 N/mm was obtained using the CBBM method for mode II pre-crack

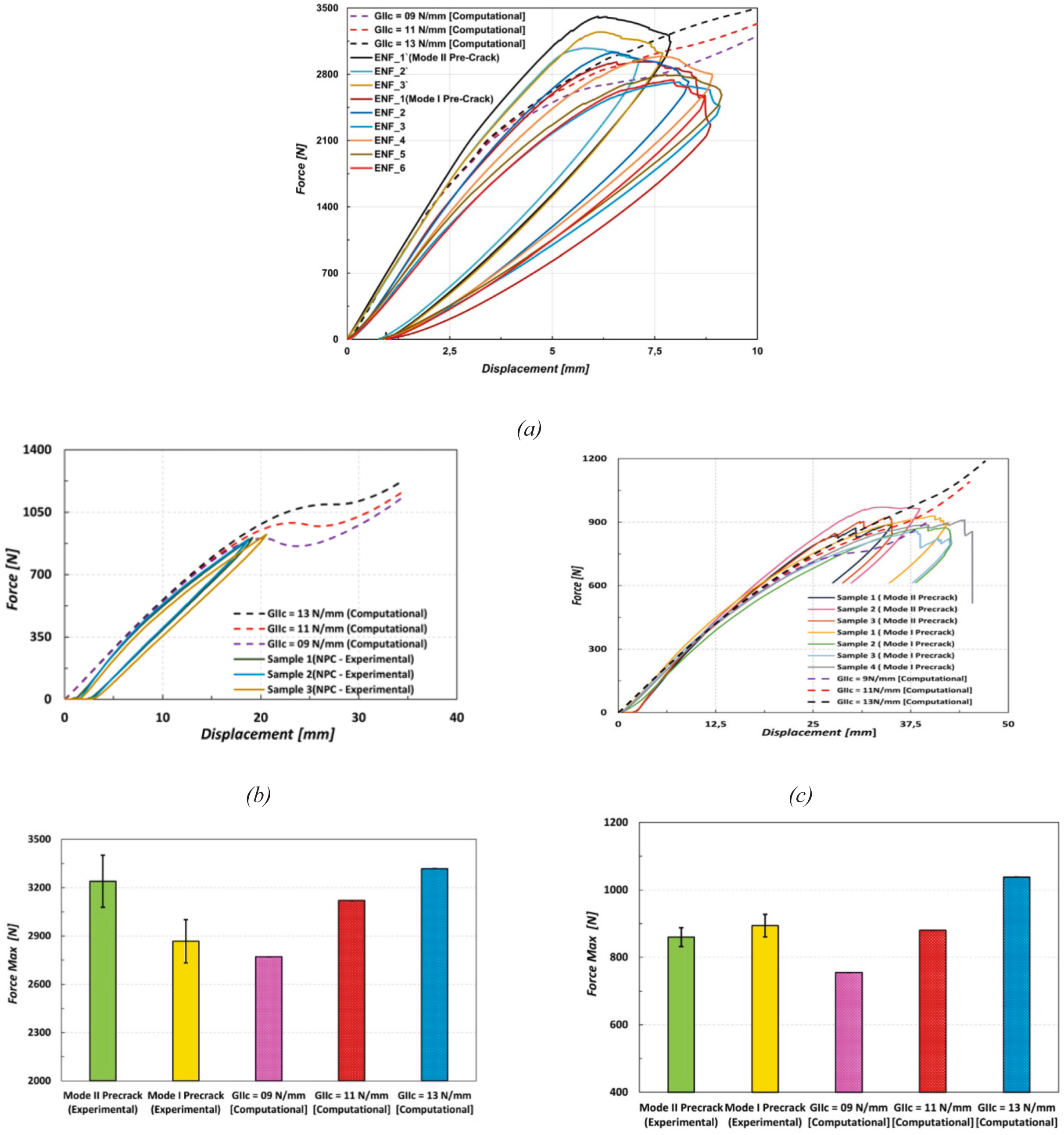

(a)

(b)

(c)

(d)

(e)

Fig. 11. Comparison of force and displacement experimental results to computational studies (a) ENF Pre-cracked Specimens (either in Mode I or Mode II), (b) Mode II Non-pre-cracked CELS specimens force–displacement response, (c) CELS Pre-cracked Specimens (either in Mode I or Mode II). Comparison of maximum load for pre-cracked specimens for (d) ENF specimens, (e) CELS specimens.

Table 3
Final cohesive properties used in FE modeling [36,66,67].

$E = E_{nn}$ [MPa]	$G = E_{ss}$ [MPa]	G_{IC} [N/mm]	G_{IIC} [N/mm]	σ_n [MPa]	σ_t [MPa]	η	s
1520	565	3.05	11.2	35	35	1.73	0.00001

ENF tests, respectively. These results from the Mode II pre-cracked specimens using apparent crack length are appropriate for conservative fracture characterization.

- The mode of pre-cracking has a significant influence on the mode II fracture energy. Mode II pre-cracking results in a lower value of G_{IIC}, whereas mode I pre-cracking captures the upper-bound fracture resistance of the adhesive layer. Mode I pre-cracked specimens (CELS and ENF) consistently exhibit higher G_{IIC} values compared to Mode II pre-cracked specimens, a difference governed by the morphology and extent of the initial FPZ. Specifically, Mode I pre-cracking produces a crack tip with a localized initial FPZ, which promotes intense plastic deformation and shear cracks during the final fracture phase, dissipating extra strain energy. Mode I pre-cracking exhibits a localized FPZ, which subsequently evolves into a shear-dominant FPZ for G_{IIC}, as observed during actual testing. In contrast, an extensive shear-driven FPZ is already present in Mode II pre-cracked specimens. This pre-existing FPZ also influences the global stiffness response, allowing the displacement behavior to be captured accordingly. Mode II pre-cracking generates a broader and more diffuse FPZ, resulting in reduced strain energy release rate, which yields lower G_{IIC} values.

The findings of this study conclude that pre-cracking and compliance effects should be appropriately considered for an effective Mode II characterization and design of adhesively bonded joints. For conservative results, a mode II pre-crack should be used, and effective crack length based methods (CBTE and CBBM) are more appropriate in cases where there are large FPZs.

CRediT authorship contribution statement

Ishan Manoj: Writing – original draft, Visualization, Validation, Methodology, Investigation, Formal analysis, Data curation, Conceptualization. **Daniel Bernardes de Castro:** Writing – review & editing, Validation, Investigation, Formal analysis, Data curation. **John-Alan Pascoe:** Writing – review & editing, Visualization, Supervision, Resources, Methodology, Funding acquisition, Conceptualization. **René Alderliesten:** Writing – review & editing, Visualization, Supervision, Resources, Methodology, Funding acquisition, Conceptualization.

Funding

The author(s) received financial support for the research, authorship, and/or publication of this article, which has been acknowledged in the manuscript.

Declaration of competing interest

The authors declare that they have no known competing financial interests or personal relationships that could have appeared to influence the work reported in this paper.

Acknowledgement

The project was carried out with a subsidy from the TSH Aircraft Manufacturing scheme of the Ministry of Economic Affairs, implemented by the Netherlands Enterprise Agency (RVO).

Appendix A. Supplementary data

Supplementary data to this article can be found online at https://doi.org/10.1016/j.engfracmech.2026.112252.

Data availability

Data will be made available on request.

References

[1] Pascoe JA, Alderliesten RC, Benedictus R. Methods for the prediction of fatigue delamination growth in composites and adhesive bonds - a critical review. Engng Fract Mech 2013;112–113:72–96. https://doi.org/10.1016/j.engfracmech.2013.10.003.

[2] Jeevi G, Nayak SK, Abdul KM. Review on adhesive joints and their application in hybrid composite structures. J Adhes Sci Technol 2019;33:1497–520. https://doi.org/10.1080/01694243.2018.1543528.

[3] Manoj I, Jain A. International Journal of Adhesion and Adhesives Strength improvement and failure analysis of dissimilar FDM printed single-lap joints with tailored interface geometry. Int J Adhes Adhes 2025;136:103876. https://doi.org/10.1016/j.ijadhadh.2024.103876.

[4] Manoj I, Kumar S, Jain A. A numerical study on stress mitigation in through-thickness tailored bi-adhesive single-lap joints. J Adhes Sci Technol 2023;37:3652–86. https://doi.org/10.1080/01694243.2023.2217674.

[5] Chaves FJP, Da Silva LFM, De Moura MFSF, Dillard DA, Esteves VHC. Fracture mechanics tests in adhesively bonded joints: a literature review. J Adhes 2014;90:955–92. https://doi.org/10.1080/00218464.2013.859075.

[6] C das Neves PJ, M da Silva LF, Adams RD. Analysis of mixed adhesive bonded joints part I: theoretical formulation. J Adhes Sci Technol 2009;23:1–34. https://doi.org/10.1163/156856108X336026.

[7] Pascoe JA, Alderliesten RC, Benedictus R. On the relationship between disbond growth and the release of strain energy. Engng Fract Mech 2015;133:1–13. https://doi.org/10.1016/j.engfracmech.2014.10.027.

[8] Álvarez D, Guild FJ, Kinloch AJ, Blackman BRK. Partitioning of mixed-mode fracture in adhesively-bonded joints: experimental studies. Engng Fract Mech 2018;203:224–39. https://doi.org/10.1016/j.engfracmech.2018.04.032.

[9] Pérez-Galmés M, Renart J, Sarrado C, Brunner AJ, Rodríguez-Bellido A. Towards a consensus on mode II adhesive fracture testing: Experimental study. Theor Appl Fract Mech 2018;98:210–9. https://doi.org/10.1016/j.tafmec.2018.09.014.

[10] ASTM D7905 Test Method for Determination of the Mode II Interlaminar Fracture Toughness of Unidirectional Fiber-Reinforced Polymer Matrix Composites 2014. https://doi.org/10.1520/D7905_D7905M-14.

[11] Fibre-reinforced plastic composites — Determination of the mode II fracture resistance for unidirectionally reinforced materials using the calibrated end-loaded split (C-ELS) test and an effective crack length approach IS0 15114. 2014.

[12] Wang W, De Freitas ST, Poulis JA, Zarouchas D. A review of experimental and theoretical fracture characterization of bi-material bonded joints. Compos B Engng 2021;206. https://doi.org/10.1016/j.compositesb.2020.108537.

[13] Ebrahimi MT, Khaji Z, Fakoor M. On mixed-mode fracture of brittle orthotropic solids: a novel micromechanical damage model. Engng Fract Mech 2025;313. https://doi.org/10.1016/j.engfracmech.2024.110628.

[14] Toolabi M, Blackman BRK. Guidelines for selecting the dimensions of adhesively bonded end-loaded split joints: an approach based on numerical cohesive zone length. Engng Fract Mech 2018;203:250–65. https://doi.org/10.1016/j.engfracmech.2018.05.019.

[15] Blackman BRK, Brunner AJ, Williams JG. Mode II fracture testing of composites: a new look at an old problem. Engng Fract Mech 2006;73:2443–55. https://doi.org/10.1016/j.engfracmech.2006.05.022.

[16] Liu (Hannah) H, Qi G, Renaud G, Li G, Li (Lucy) C. Application of the effective crack length method to model delamination of unidirectional composite laminates under Mode II shear loadings. Composites, Part C: Open Access 2023;12. https://doi.org/10.1016/j.jcomc.2023.100401.

[17] Carlsson LA, Gillespie JW, Pipes RB. On the analysis and design of the end notched flexure (ENF) specimen for mode II testing. J Compos Mater 1986;20:594–604. https://doi.org/10.1177/002199838602000606.

[18] Fernlund G, Spelt JK. MIXED-MODE FRACTURE ADHESIVE CHARACTERIZATION OF JOINTS. vol. 50. 1994.

[19] Davies P. Influence of ENF specimen geometry and friction on the mode II delamination resistance of carbon/PEEK. J Thermoplast Compos Mater 1997;10:353–61. https://doi.org/10.1177/089270579701000404.

[20] Brunner AJ. Experimental aspects of Mode I and Mode II fracture toughness testing of ®bre-reinforced polymer-matrix composites. n.d.

[21] Brunner AJ, Blackman BRK, Williams JG. Calculating a damage parameter and bridging stress from GIC delamination tests on fibre composites. Compos Sci Technol 2006;66:785–95. https://doi.org/10.1016/j.compscitech.2004.12.040.

[22] Blackman BRK, Kinloch AJ, Paraschi M. The determination of the mode II adhesive fracture resistance, GIIC, of structural adhesive joints: an effective crack length approach. Engng Fract Mech 2005;72:877–97. https://doi.org/10.1016/j.engfracmech.2004.08.007.

[23] de Moura MFSF, de Morais AB. Equivalent crack based analyses of ENF and ELS tests. Engng Fract Mech 2008;75:2584–96. https://doi.org/10.1016/j.engfracmech.2007.03.005.

[24] de Moura MFSF, Campilho RDSG, Gonçalves JPM. Pure mode II fracture characterization of composite bonded joints. Int J Solids Struct 2009;46:1589–95. https://doi.org/10.1016/j.ijsolstr.2008.12.001.

[25] de Moura MFSF, Silva MAL, de Morais AB, Morais JJL. Equivalent crack based mode II fracture characterization of wood. Engng Fract Mech 2006;73:978–93. https://doi.org/10.1016/j.engfracmech.2006.01.004.

[26] Sarrado C, Turon A, Costa J, Renart J. On the validity of linear elastic fracture mechanics methods to measure the fracture toughness of adhesive joints. Int J Solids Struct 2016;81:110–6. https://doi.org/10.1016/j.ijsolstr.2015.11.016.

[27] Sarrado C, Turon A, Renart J, Costa J. An experimental data reduction method for the mixed mode bending test based on the J-integral approach. Compos Sci Technol 2015;117:85–91. https://doi.org/10.1016/j.compscitech.2015.05.021.

[28] Sun F, Lißner M, Petrinic N, Blackman BRK. Universal slope-based J-integral methods for characterization of the mode I, mode II and mixed mode I/II fracture behaviour of adhesively bonded interfaces. Compos Sci Technol 2024;252. https://doi.org/10.1016/j.compscitech.2024.110611.

[29] Sun F, Blackman BRK. A DIC method to determine the Mode I energy release rate G, the J-integral and the traction-separation law simultaneously for adhesive joints. Engng Fract Mech 2020;234. https://doi.org/10.1016/j.engfracmech.2020.107097.

[30] Demiral M, Kadioglu F. Failure behaviour of the adhesive layer and angle ply composite adherends in single lap joints: a numerical study. Int J Adhes Adhes 2018;87:181–90. https://doi.org/10.1016/j.ijadhadh.2018.10.010.

[31] Kadioglu F, Demiral M. Failure behaviour of the single lap joints of angle-plied composites under three point bending tests. J Adhes Sci Technol 2020;34:531–48. https://doi.org/10.1080/01694243.2019.1674101.

[32] Quan D, Wang G, Zhao G, Alderliesten R. On the fracture behaviour of aerospace-grade Polyether-ether-ketone composite-to-aluminium adhesive joints. Compos Commun 2022;30. https://doi.org/10.1016/j.coco.2022.101098.

[33] Carbas RJC, Marques EAS, da Silva LFM. The influence of epoxy adhesive toughness on the strength of hybrid laminate adhesive joints. Appl Adhes Sci 2021;9. https://doi.org/10.1186/s40563-020-00132-5.

[34] Morgado MA, Carbas RJC, dos Santos DG, da Silva LFM. Strength of CFRP joints reinforced with adhesive layers. Int J Adhes Adhes 2020;97. https://doi.org/10.1016/j.ijadhadh.2019.102475.

[35] Ramezani F, Nunes PDP, Carbas RJC, Marques EAS, da Silva LFM. The joint strength of hybrid composite joints reinforced with different laminates materials. J Adv Join Proc 2022;5. https://doi.org/10.1016/j.jajp.2022.100103.

[36] Sun F, Wang Q, Blackman BRK. Validity of LEFM to measure the Mode II and mixed Mode I/II fracture toughness of adhesively bonded CFRP. Compos A Appl Sci Manuf 2025;192. https://doi.org/10.1016/j.compositesa.2025.108777.

[37] Ameli A, Papini M, Schroeder JA, Spelt JK. Fracture R-curve characterization of toughened epoxy adhesives. Engng Fract Mech 2010;77:521–34. https://doi.org/10.1016/j.engfracmech.2009.10.009.

[38] Lima RAA, Tao R, Bernasconi A, Carboni M, Carrere N, Teixeira de Freitas S. Uncovering the toughening mechanisms of bonded joints through tailored CFRP layup. Compos B Engng 2023;263. https://doi.org/10.1016/j.compositesb.2023.110853.

[39] Tijs BHAH, Abdel-Monsef S, Renart J, Turon A, Bisagni C. Characterization and analysis of the interlaminar behavior of thermoplastic composites considering fiber bridging and R-curve effects. Compos A Appl Sci Manuf 2022;162. https://doi.org/10.1016/j.compositesa.2022.107101.

[40] Reis JP, de Moura MFSF, Moreira RDF. Extension of the crack equivalent method applied to mode II fracture of thermoplastic composites bonded joints using the ENF test. Compos Struct 2025;352. https://doi.org/10.1016/j.compstruct.2024.118687.

[41] Moore DR, Pavan A, Williams JG, Fracture E. Mechanics testing methods for polymers, adhesives and composites. Eur. Struct. Integ. Soc 2001;28:3–375.

[42] Davies P, Sims GD, Blackman BRK, Brunner AJ, Kageyama K, Hojo M, et al. Comparison of test configurations for determination of mode II interlaminar fracture toughness results from international collaborative test programme. Plast, Rubber Compos 1999;28:432–7. https://doi.org/10.1179/146580199101540600.

[43] Álvarez D, Blackman BRK, Guild FJ, Kinloch AJ. Mode I fracture in adhesively-bonded joints: a mesh-size independent modelling approach using cohesive elements. Engng Fract Mech 2014;115:73–95. https://doi.org/10.1016/j.engfracmech.2013.10.005.

[44] Sawada T, Kawamori T, Matsunaga M. Energy release rate estimation method for debonding analysis of single-lap adhesively bonded joints considering practicality and simplicity. Engng Fract Mech 2025;326. https://doi.org/10.1016/j.engfracmech.2025.111432.

[45] Jia R, Zhao L, Curti R, Gong X. Determination of pure mode-I fracture toughness of multidirectional composite DCB specimens. Engng Fract Mech 2021;252. https://doi.org/10.1016/j.engfracmech.2021.107776.

[46] Sun F, Zhang R, Blackman BRK. Determination of the mode I crack tip opening rate and the rate dependent cohesive properties for structural adhesive joints using digital image correlation. Int J Solids Struct 2021;217–218:60–73. https://doi.org/10.1016/j.ijsolstr.2021.01.034.

[47] Lima RAA, Drobiazko M, Bernasconi A, Carboni M. On crack tip localisation in quasi-statically loaded, adhesively bonded double cantilever beam specimens by acoustic emission. Theor Appl Fract Mech 2022;118. https://doi.org/10.1016/j.tafmec.2022.103286.

[48] Zhang Y, Shi J, Zheng J. A method of fracture toughness JIC measurement based on digital image correlation and acoustic emission technique. Mater Des 2021;197. https://doi.org/10.1016/j.matdes.2020.109258.

[49] Pérez-Galmés M, Renart J, Sarrado C, Rodríguez-Bellido A, Costa J. A data reduction method based on the J-integral to obtain the interlaminar fracture toughness in a mode II end-loaded split (ELS) test. Compos A Appl Sci Manuf 2016;90:670–7. https://doi.org/10.1016/j.compositesa.2016.08.020.

[50] Salamat-Talab M, Kazemi H, Mahdavi M. Influence of yarn bundle orientation and areal density on the interlaminar fracture toughness of ENF composites. Engng Fract Mech 2025;315. https://doi.org/10.1016/j.engfracmech.2025.110806.

[51] HexPLy 8552 Data Sheet. www.hexCel.com. Physical Properties. n.d.

[52] Yudhanto A, Alfano M, Lubineau G. Surface preparation strategies in secondary bonded thermoset-based composite materials: a review. Compos A Appl Sci Manuf 2021;147. https://doi.org/10.1016/j.compositesa.2021.106443.

[53] 3M Scotch-Weld Structural Adhesive Film AF 163-2. n.d.

[54] Ramezani F, Ayatollahi MR, Akhavan-Safar A, da Silva LFM. A comprehensive experimental study on bi-adhesive single lap joints using DIC technique. Int J Adhes Adhes 2020;102:102674. https://doi.org/10.1016/J.IJADHADH.2020.102674.

[55] Arouche MM, Pavlovic M. Experimental and numerical analysis of the effect of temperature on the mode I and mode II delamination of glass fiber woven composites. Compos B Engng 2025;293. https://doi.org/10.1016/j.compositesb.2025.112131.

[56] Gfrerrer M, Koss V, Wiener J, Schuecker C, Brunner AJ, Pinter G. Comparing Mode I, Mode II and Mixed-Mode I/II interlaminar fracture toughness of glass and carbon fiber reinforced polymer laminates with the same epoxy matrix system. Engng Fract Mech 2025;320. https://doi.org/10.1016/j.engfracmech.2025.111009.

[57] Zhao LC, Yuan L, Wang ZR. Influence of 3D printing parameters on the fracture behavior of adhesive joints under mode II quasi-static loading: experimental and numerical insights. J Adhes 2025. https://doi.org/10.1080/00218464.2025.2602654.

[58] De Baere I, Jacques S, Van Paepegem W, Degrieck J. Study of the mode i and mode II interlaminar behaviour of a carbon fabric reinforced thermoplastic. Polym Test 2012;31:322–32. https://doi.org/10.1016/j.polymertesting.2011.12.009.

[59] Wang Y, Williams JG. Corrections for Mode II fracture toughness specimens of composites materials. vol. 43. 1992.

[60] Dassault Systèmes Simulia Corp. S. ABAQUS/CAE 2024.

[61] Manoj I, Jain A. Fracture behavior and strength enhancement of 3D-printed stepped-lap bonded joints using geometrically graded interfaces: experimental validation and damage modelling. J Adhes Sci Technol 2025:1–31. https://doi.org/10.1080/01694243.2025.2575812.

[62] Manoj I, Kumar Shah A, Jain A. Strength and failure assessments of 3D printed PLA single lap joints: Experimental and numerical analysis. Engng Fail Anal 2024;161. https://doi.org/10.1016/j.engfailanal.2024.108257.

[63] Dávila CG, Weeks S, Czabaj M. Propagation rate transients in J-controlled fatigue characterization of adhesives. Int J Fatigue 2024;185. https://doi.org/10.1016/j.ijfatigue.2024.108377.

[64] Wanthal S, Schaefer J, Justusson B, Hyder I, Engelstad S, Rose C. Paper Number: Session Topic: Verification & Validation of Progressive Damage/Failure Analysis for Stiffened Composite Structures Title: Verification and Validation Process for Progressive Damage and Failure Analysis Methods in the NASA Advanced Composites Consortium. n.d.

[65] da Silva LFM, das Neves PJC, Adams RD, Spelt JK. Analytical models of adhesively bonded joints—Part I: Literature survey. Int J Adhes Adhes 2009;29:319–30. https://doi.org/10.1016/J.IJADHADH.2008.06.005.

[66] Manoj I, de Castro DB, Pascoe J-A, Alderliesten R. How differences in fracture process zone behavior prevent transferability of mixed-mode fracture toughness measurements in toughened adhesive CFRP joints. Theor Appl Fract Mech 2026;145:105617. https://doi.org/10.1016/j.tafmec.2026.105617.

[67] Morgado MA, Carbas RJC, Marques EAS, da Silva LFM. Reinforcement of CFRP single lap joints using metal laminates. Compos Struct 2019;230. https://doi.org/10.1016/j.compstruct.2019.111492.